November 2014

Evolution of Off-Fault Deformation along Analog Strike-Slip Faults

Alexandra E. Hatem
University of Massachusetts Amherst

EVOLUTION OF OFF-FAULT DEFORMATION ALONG ANALOG STRIKE-SLIP FAULTS

A Thesis Presented

by

ALEXANDRA ELISE HATEM

MASTER OF SCIENCE

September 2014

Department of Geosciences

EVOLUTION OF OFF-FAULT DEFORMATION ALONG ANALOG STRIKE-SLIP FAULTS

A Thesis Presented

by

ALEXANDRA ELISE HATEM

Approved as to style and content by:

_____

Michele Cooke, Chair

_____

Elizabeth Madden, Member

_____

Laurie Brown, Member

_____

Sheila Seaman, Acting Department Head

Geosciences

ABSTRACT

EVOLUTION OF OFF-FAULT DEFORMATION ALONG ANALOG STRIKE-SLIP FAULTS

SEPTEMBER 2014

ALEXANDRA ELISE HATEM, B.A. WELLESLEY COLLEGE

M.S., UNIVERSITY OF MASSACHUSETTS AMHERST

Directed by: Professor Michele Cooke

Strike-slip faults evolve to accommodate more fault slip, resulting in less off-fault deformation. In analog experiments, the measured fault slip to off-fault deformation ratios are similar to those measured in crustal strike-slip systems, such as the San Andreas fault system. Established planar faults have the largest fault slip to off-fault deformation ratio of ~0.98. In systems without a pre-existing fault surface, crustal thickness and basal detachment conditions affect shear zone width and roughness. However, once the applied plate displacement is 1-2 times the crustal thickness, partitioning of deformation between fault slip and off-fault distributed shear is >0.90, regardless of the basal boundary conditions. In addition, at any moment during the evolution of the analog fault system, the ratio of fault slip to off-fault deformation is larger than the cumulative ratio. We also find that the upward and lateral propagation of faults as an active shear zone developing early in the experiments has greater impact on the system's strike-slip efficiency than later interaction between non-collinear fault segments. For bends with stepover distance of twice the crustal thickness, the fault slip to off-fault deformation ratio increases up to ~0.80-0.90, after applied plate displacement exceeds twice the crustal thickness. Propagation of new oblique-slip faults around sharp

restraining bends reduces the overall off-fault deformation within the fault system. In contrast, fault segments within gentle restraining bends continue to slip and the propagation of new oblique-slip faults have less effect on the system's efficiency than for sharp restraining bends.

PREFACE

In this thesis, I present two distinct chapters, both satisfying the broad topic "Evolution of off-fault deformation along analog strike-slip faults." Chapter 1, entitled "Strike-slip efficiency of restraining bends observe in wet kaolin analog experiments" aims to characterize the structural and mechanical evolution of idealized stepovers. Using wet kaolin modeling, we tested a variety of plausible kink angles in a parametric study to decipher how stepovers evolve over time with respect to their initial geometric deviation from plate motion. This paper will be submitted to the Journal of Geophsyical Research by the end of 2014, and will be authored by Alex Hatem, Michele Cooke and Elizabeth Madden. Chapter 2, entitled "Strain localization and efficiency in wet kaolin experiments of initiating strike-slip faults," also uses wet kaolin analog modeling as an experimental approach. This study focuses on the initiation of a whole strike-slip fault, as opposed to a singular, preexisting stepover as discussed in chapter 1. In that work, we monitor the spatial and temporal distribution of strain during strike-slip initiation as we categorize a stepwise behavior observed in the development of all tested faults, which agrees well with observations of crustal systems. Chapter 2 will be submitted to Earth and Planetary Science Letters by the end of summer 2015, and will be authored by at least Alex Hatem and Michele Cooke. These chapters are separate entities relating to the similar overall topic of strike-slip fault evolution, and are presented as two separate manuscripts for publication in this two chapter thesis.

TABLE OF CONTENTS

Page

LIST OF TABLES

Table Page

LIST OF FIGURES

CHAPTER 1

STRIKE-SLIP EFFICIENCY OF RESTRAINING BENDS OBSERVED IN WET KAOLIN ANALOG EXPERIMENTS

1.1 Abstract

Restraining bends within strike-slip fault systems are interpreted to evolve over time, by propagation of new faults and abandonment of fault segments. Analog modeling using wet kaolin, a material that scales to the Earth's crust in length and strength, allows for qualitative and quantitative observations of restraining bend evolution. In general, these analog experiments demonstrate that restraining bends overcome initial inefficiencies by abandoning poorly oriented structures in favor of propagating new, inwardly dipping, oblique-slip faults well oriented to accommodate convergence within the bend. We model restraining bends with angles of $\theta = 0^\circ$ to 30° to study how θ affects this evolution. Particle Image Velocimetry (PIV) analysis reveals that new oblique-slip faults grow on one or both sides of all restraining bends with $\theta > 0^\circ$. Early in experiments, faults within high angle restraining bends ($\theta \geq 20^\circ$) exhibit less strike-slip than faults within low angle restraining bends ($\theta < 20^\circ$) We quantify *strike-slip efficiency* of the system as the percentage of strike-slip on faults within the restraining bend relative to the applied strike-slip plate displacement. Using this terminology, bends with small θ initially have higher strike-slip efficiency than bends with large θ. Propagating a new fault increases the efficiency of all systems with $\theta > 0^\circ$. However, the timing of the first new fault to propagate is not dependent on strike-slip efficiency. Instead, the first fault propagates at the same threshold accumulated convergence of 5.3 mm in all experiments. We further observe that all systems reach a steady strike-slip efficiency of 80 % after 50

mm of applied plate displacement. After this steady strike-slip efficiency is reached, the propagation and linkage of new faults continues, and the fault system maintains strike-slip efficiency near 80 %. These findings suggest that restraining bends are mechanically inefficient structures that evolve to improve strike-slip efficiency, and that the mechanics of this evolution are controlled by convergence within the bend. Experimental restraining bends presented here provide the asymmetric fault growth, asymmetric topographic gradient, fault growth evolution and strike-slip efficiency of crustal strike-slip systems.

1.2 Introduction

Restraining bends occur along strike-slip faults due to significant changes in strike. Such deviations in strike affect how strain is accommodated, if the stress orientation remains constant through the region (e.g. Fialko et al., 2005; Titus et al., 2007; Shelef and Oskin, 2010; Cooke and Dair, 2011; McGill et al., 2013). Presumably, if the change in fault strike is large, the existing strike-slip faults within the restraining bend will be poorly oriented relative to the direction of the regional maximum compressive stress to accommodate all or most of the resulting strain as strike-slip (e.g. Wakabayashi et al., 2004; Gomez et al., 2007). Because of this, restraining bends may be characterized as mechanically inefficient structures (Cooke and Dair, 2011; Cooke et al., 2013).

However, restraining bends may evolve over time to become more mechanically efficient (Cooke et al., 2013). Strike-slip accommodated along faults within a restraining bend may increase as structures are abandoned and new, more favorably oriented faults grow (Wakabayashi et al., 2004; Wakabayashi 2007, Cooke et al., 2013). For instance, the Dead Sea Fault of Lebanon and southwest Syria exhibits a long history of fault

initiation and abandonment as strain partitioning within the system has evolved over time (Gomez et al., 2003; Gomez et al., 2007; Figure 1A) In the Dead Sea Fault system, strike-slip rates vary spatially and temporally and convergence is accommodated adjacent to the restraining bend as uplift along the Lebanon Range (Figure 1A). Additionally, the strike-slip Denali Fault north of the Aleutian arc subduction zone includes a restraining bend, which contains faults that accommodate convergence resulting in uplift of the Alaska Range (Haeussler 2008).

Complex deformational processes, such as those along the Dead Sea and Denali faults, occur over geologic time, yet can be modeled in analog experiments over several hours. Analog modeling has been conducted for over a century to study many tectonic environments, including compressional, extensional, transpressional and accretionary systems (e.g. Cadell 1889; Oertel, 1965; Cloos 1968; Withjack et al., 1995; Ackerman et al., 2001; McClay and Bonora, 2001; Schlische et al., 2002; Del Castello et al 2004; Malavieille 2010; Henza et al., 2010; Mitra and Paul, 2011; Paul and Mitra, 2013; Cooke et al., 2013; Curren and Bird, 2014). For example, sandbox models of stepovers by McClay and Bonora (2001) show a progression of reverse faulting inward from the fault shoulders toward the center of the step, where significant uplift occurs. These authors correlate different fault geometries and topography with restraining stepover geometry. Using analog models with stiffer, drier clay underlying less rigid, wetter clay Mitra and Paul (2011) find that uplift patterns depend on initial fault geometry and secondary fault propagation. Laser scans of the models show that elongated, spindle shaped regions of uplift form within restraining bends with low θ, and more rectangular regions of uplift form within high θ bends. Cooke et al. (2013) measure uplift, surface strain, and fault slip

during the evolution of restraining bends with θ = 45° and various stepover distances, a parameter defined as the lateral distance between the two parallel fault segments away from the bend. They find that wide stepovers are initially less strike-slip efficient than narrow stepovers. As the faults evolve within these restraining bends, the difference in strike-slip efficiency decreases (Cooke et al., 2013).

The claybox models presented here extend these analyses by utilizing Particle Image Velocimetry (PIV) analysis. PIV allows the complete horizontal strain field to be captured by tracking pixels in successive images (e.g. Adrian and Westerweel, 2011). This approach captures slip at the resolution of individual pixels and improves the density and wealth of slip data collected in the claybox experiments. Utilizing PIV, we map active faults, quantify how fault systems accommodate applied displacement, and track how strike-slip efficiency changes as the fault system evolves. We compare the evolving strike-slip efficiency of restraining bends with different θ by calculating the ratio of strike-slip along the fault within the bend to the applied displacement.

1.3 Methods

1.3.1 Claybox

The claybox is a motor-controlled, table-top, laboratory rig designed to simulate crustal faulting (Figure 1B, 1C). Experiments in this study are conducted with a clay thickness of 2.5 cm. The clay lies atop two steel, basal plates that reflect the restraining bend geometry of a particular experiment. This geometry is defined by stepover distance and θ (Figure 1D). We keep stepover distance constant across all experiments at 5 cm and vary θ from 0˚ to 30˚ at 5˚ intervals. These geometries reflect restraining bends observed

in the crust, such as the low angle bends along the Altai Gobi Fault (e.g. Cunningham 2007) and the high angle bend along the southern San Andreas Fault (e.g. Yule and Sieh 2003). We did not test a 5˚restraining bend because the length of such a low angle restraining bend exceeds the size of the claybox.

We cut one vertical fault in the clay using an electrified probe following a template that matches the basal plate geometry. The electrified probe effectively breaks attractive forces within the kaolin, providing a neat cut with minimal puckering of the clay. The surface of the clay has the same geometry as the basal plate. Reference lines are pressed into the surface of the clay ~1 cm apart and perpendicular to the fault outside of the bend. These lines bend as the clay strains, and are later displaced as the fault slips, providing the observer with a way to manually track deformation during the experiment. Finally, red and black sand is sprinkled on top of the clay for the Particle Image Velocimetry (PIV) analysis (Figure 1C, 1D).

One basal plate remains stationary while the other moves laterally via a computer controlled stepper motor at 0.5 mm/min. Photographs record the experiment from above the claybox at one minute intervals (Figure 1A). An experiment lasts ~3 hours and is equivalent to about 1 my of crustal deformation, if 45 mm/yr plate rates are assumed (e.g. Cooke and van der Elst, 2012; Demets et al., 2010).

1.3.2 Modeling Material

Both wet kaolin and dry sand have been used successfully in analog modeling of restraining bends. Eisenstadt and Sims (2005) compared these two materials and found that wet kaolin allows reactivation of discrete faults. In contrast, dry sand favors the development of broad deformation zones, with many newly grown faults. Schlische et al.

(2002) prefer wet kaolin over dry sand, as clay allows for the development of a higher number of narrow, discrete faults (Withjack and Callaway, 2002).

We use wet kaolin in these models because we are interested in studying the evolution of discrete faults. In addition, wet kaolin has properties that scale to reflect the rheology of Earth's crust (Eisenstadt and Sims, 2005; Cooke and van der Elst, 2012). Prior to failure, it deforms as a bi-viscoelastic Burger's material, which reflects the long-term behavior of the crust (Cooke and van der Elst, 2012). At failure, wet kaolin demonstrates the rate-and-state behavior of many crustal faults (Cooke and van der Elst, 2012). Shear strength in wet kaolin is independent of strain rate and correlates instead to normal compression, as do rocks within the upper ~15 km of the Earth (Cooke and van der Elst, 2012).

Prior to every experiment, the wet kaolin shear strength is tested to ensure that the clay shear strength scales to crustal shear strength. Proper scaling allows observations of the experimental restraining bends to be linked to crustal restraining bends. The target strength of the clay is 90-115 Pa. The kaolin is scaled to the Earth's crust using the following formula:

$$\frac{S_m}{S_P} = \frac{\rho_m}{\rho_p}\frac{z_m}{z_p}\frac{g_m}{g_p}\frac{\Phi_m}{\Phi_p} \qquad \text{Equation 1}$$

where S is strength, ρ is density, z is length, g is acceleration due to gravity, and □ is the coefficient of internal friction; the subscript m stands for model (i.e. claybox), and the subscript p stands for prototype (i.e. continental crust) (Henza et al., 2010; Cooke et al., 2013). The density of the kaolin is 1.6 g/cm^3 and the density of continental crust is 2.65 g/cm^3. The shear strength of the crust is 10-20 MPa.

Friction is the same for both the kaolin and the crust, with a range of 0.55-0.85 (Schlishe et al., 2002), and g is also the same for both. Thus, Equation 1 simplifies to:

$$S_r = \rho_r z_r \quad \text{Equation 2}$$

Here, S_r is the strength scaling ratio, ρ_r is the density scaling ratio, and z_r is the length scaling ratio (Henza et al., 2010; Cooke et al., 2013). S_m is calculated using a fall cone test, in which a calibrated cone is dropped from a recorded height into a small container of kaolin. The depression depth of the cone within the wet kaolin correlates to pre-determined values of S_m (DeGroot and Lunne, 2007) and is controlled by the water content (e.g. Eisenstadt and Sims, 2005; Cooke and van der Elst 2012), which is typically 65-70%. Using Equation 2, the length scaling is such that 1 cm in the clay is equivalent to 0.75-1.4 km of continental crust. On average, the analog system is five orders of magnitude smaller than a crustal system. Kaolin aliquots sampled before and after the experiment are baked for one week after the experiment to measure any changes in water content during the experiment. However, in general, water loss during experiments is minimal (~3%) and does not affect the rheology of the wet kaolin.

1.3.3 Particle Image Velocimetry (PIV)

Particle Image Velocimetry (PIV) is a technique used to track pixels over multiple photographs taken every 1 min throughout the experiment (e.g. Adam et al. 2005; Slominski et al., 2007). The color contrast provided by sprinkling both red and black sand on top of the wet kaolin increases PIV accuracy. The photographs provide a typical resolution of 90 pixels/cm. Each image is corrected for camera lens effects. Displacement of the sand particles between successive images is measured in fixed 25 x 25 pixel windows.

To measure strike-slip along a fault without PIV, one manually maps the displacements along faults from the offset reference lines (Figure 2A). In contrast, PIV enables automatic measurements of the displacement from one image to the next, from which a velocity map is built (Figure 2B). Gradients in the velocity field are used to identify both incipient and active faults (Figure 1B). We calculate shear strain (ε_{xy}) rate from the gradient of the velocity map (Figure 2C) and identify faults where ε_{xy}/min > 0.3/min. We determined this critical ε_{xy} rate by finding the rate above which offset is localized along a straight, strike-slip fault. Because PIV provides the complete horizontal displacement field, both strike-slip and dip-slip displacement can be calculated as the gradients of the displacement in the x- and y-directions, respectively (Figure 2D).

Comparing Figures 2A and 2D shows the power of characterizing fault systems using PIV. The manual fault map (Figure 2A) shows two active faults initiating from the left side of restraining bend, whereas the fault style map from the PIV analysis (Figure 2D) reveals that only one of those faults is active at this time. The fault style map also reveals that the active fault links to the fault on the right of the restraining bend and is slipping obliquely; this information is not available from the manual fault mapping. In addition, using PIV is superior to using laser scans to capture deformation because it is accomplished with less set-up time and it provides a more detailed map of strain (90 pixels/cm compared to one line/cm for laser scans). In these ways, PIV more readily provides rich data for analyzing fault system evolution.

Furthermore, PIV does not require that the experiment be paused, as is necessary to acquire laser scans. Figure 3A compares strike-slip rates acquired using PIV both with and without stopping the applied displacement for laser scans and reveals that the strike-

slip rate decreases after each scan, suggesting that the shear stress decreases on the fault during this pause. This observation is supported by the fact that the Maxwell viscous relaxation time of wet kaolin is 15 minutes (Cooke and van der Elst, 2012), which is shorter than the 20 minutes required for each laser scan. When applied displacement recommences, the shear stress on the fault no longer equals the shear strength of the clay. Instead, the kaolin accumulates strain until the shear stress along the fault exceeds its shear strength and induces slip. The fault in the arrested experiment has less total slip than the uninterrupted experiment (Figure 3A).

One 3D laser scan with a resolution of 380 points/cm^2 is completed after the experiment is over to avoid interfering with deformation. This scan captures the final uplift within the restraining bend. In addition, several experiments are run back to their starting position after completion of the experiment, in order to expose the fault surfaces. A laser scan of these experiments allows for dip measurements to be taken along these fault surfaces.

1.3.4 Experimental repeatability and variability in initial fault slip

To confirm the repeatability of the modeling methods, we tested the $\theta = 25°$ experiment four times under identical conditions. The temporal evolution of strike-slip rate in each of these experiments is similar (Figure 3B). The rate varies most early in each experiment, increasing from 0.05 mm/min to ~0.275 mm/min. During this initial stage, the slip rate can vary up to 20 % between experiments (~0.1 mm/min) after 10mm of plate displacement. In contrast, between 20 mm and 60 mm of plate displacement, strike-slip rates vary between experiments only by 5%.

Figure 3C shows that this variability in strike-slip rate occurs during the initial 10 mm of plate displacement in almost all experiments and is largest in low angle bends. For instance, the straight fault in the $\theta = 0°$ experiment is slipping at 0.18 mm/min after 1.8mm of plate displacement, but this rate decreases to 0.1 mm/min after ~5 mm plate displacement, then increases again. After 6 mm of applied displacement, the slip rate along the restraining bend faults in all experiments increases monotonically. These changes in strike-slip rate early in the experiments may occur because of fluid flow onto the pre-cut fault, prior to the start of applied displacement. This would temporarily reduce the shear strength of the fault and allow the strike-slip rate to increase rapidly. The initiation of fault slip may then disperse this fluid, causing the faults to stick again until shear stress along the fault increases to meet the fault strength in the absence of fluids. Although this stick-slip behavior is interesting and could be the focus of future work, we will only discuss slip after this initial stick-slip behavior in the results.

In all of the experiments presented here with $\theta > 0^{\circ}$, the first fault to propagate initiates from the same side of the restraining bend. To test whether this is related to the experimental design, we changed the typical set-up shown in Figure 4A to have the moving plate pass under the stationary plate. We observe that, regardless of which basal plate is moving, the first fault to grow initiates near the edge of the overriding plate (Figure 4A and B). This shows that the propagation of a new fault is not affected by the direction of basal plate motion, but may be affected by the heterogeneity introduced by the edge of the overriding plate. This edge may provide a detachment at which it is easier for faults to initiate. The initiation of faults from a basal detachment or heterogeneity may be observed in crustal systems, as well, as in a flower structure (e.g. Scholz, 2002). Faults

in crustal restraining bends also may initiate at a change in crustal thickness; however, crustal systems have a more pronounced step in crustal thickness in crustal systems compared to the claybox (i.e. Yule and Sieh 2003; Veenstra et al., 2006). The faults in both experiments exhibit similar strike-slip rates over the course of the experiments (Figure 4C).

1.4 Results

1.4.1 Fault evolution of restraining bends

To analyze the evolution of faults within the modeled restraining bends, we make qualitative observations from the images collected during the experiment (e.g. Figure 2A) and track the slip along the pre-cut and newly grown faults using PIV generated fault-style maps (e.g. Figure 2D). In each experiment, we identify the onset of slip localization, fault propagation, fault linkage, slip along linked faults, and fault abandonment. For animations of all experiments, please refer to the videos provided in the Supplemental Information.

Restraining bends have different fault evolution and final fault geometries depending on θ. Figure 4 compares fault system evolution within the θ = 15° and 30° experiments. In the θ = 15° experiment, the segment of the pre-cut fault within the restraining bend slips for the entire experiment, with strike- and dip-slip (Figure 5A-C). This also occurs in the other low angle restraining bend tested, with θ = 10°. However, the segment of the pre-cut in the θ = 30° restraining bend never slips (Figure 5D-F), and this is also true for the other high angle bends with θ = 20° and 25°.

In all experiments with θ > 0˚, new faults initiate from the kinks in the pre-cut fault. In the θ = 15° and 10° restraining bends, these new faults propagate only from one

kink on one side of the restraining bend. In contrast, in the higher angle experiments, new faults propagate from the kinks on both sides of the bend. In addition, the initial directions of propagation for these new faults vary in the low versus high angle bends. In experiments with $\theta < 20^{\circ}$, new faults initially propagate away from the restraining bend at 25˚ - 30˚ from the fault segment outside of the bend (e.g. Figure 5B). In experiments with $\theta \geq 20^{\circ}$, this propagation angle is less than 10° (e.g. Figure 5E). However, as these new faults continue to propagate, they eventually assume an orientation parallel to the segment of the pre-cut fault within the bend. At most, the orientation of the new fault within the bend deviates from the orientation of the pre-cut fault within the bend by 2˚.

In Figure 6, we present snapshots of the $\theta = 20^{\circ}$ restraining bend experiment in order to highlight some details of the fault system's evolution. This evolution can be observed best in the animations provided in the Supplemental Information. Within this experiment, the pre-cut fault begins to slip by predominantly strike-slip motion after 8 mm of applied plate displacement (Figure 6A). After 24 mm of plate displacement, the pre-cut fault within the restraining bend begins to slip obliquely and a new fault initiates at the left kink (fault I, Figure 6B). The entire pre-cut fault within the bend is slipping by 32 mm of plate displacement, and fault I has propagated into the bend (Figure 6C). The pre-cut segment of the fault within the restraining bend is being abandoned (Figure 6D), fault I continues to slip obliquely as it grows across the bend, and a new fault (fault II) is visible on the opposite side of the bend. By 79 mm of plate displacement, fault I has linked to the right side of the pre-cut fault on the opposite side of the bend (Figure 6E). As shown in Figure 6F, by 79 mm of applied displacement, a new fault (fault III) has initiated near fault I and the two faults are simultaneously active on one side of the bend.

We hypothesize that fault III grows as an imbricate fault, outboard of fault I. Fault II has linked to the opposite side of the restraining bend by this time. By 85 mm of plate displacement, fault III has linked to fault I and fault I has been abandoned inboard of fault III (Figure 6G). The resultant fault IV has variable strike and accommodates oblique-slip.

The structural evolution of faults within all of the experiments is summarized graphically in the fault evolution timeline shown in Figure 7. This timeline permits comparison between experiments in terms of localization of slip, fault propagation, fault linkage and fault abandonment. The evolution of faults within all modeled restraining bends also can be observed in animations provided in the Supplemental Information. In Figure 7, for each experiment, we differentiate between slip along the pre-cut fault and slip along new faults. We distinguish fault growth on opposite sides of the bend by referring to faults that grow above the overriding, moving plate versus those that grow above the underthrusting, stationary plate (Figure 7B). We number new faults by growth order within each experiment as we did in Figure 6 (e.g. fault I, II, etc).

As demonstrated by the gray lines in Figure 7, in low angle experiments ($\theta = 10°$ and 15°), slip along the pre-cut fault within the bend occurs after less applied displacement. In addition, as θ increases, the growth of fault I occurs after less applied displacement. These observations suggest that the segment of the pre-cut fault within a restraining bend with large θ is not favorably oriented to accommodate horizontally applied strike-slip by strike-slip displacement and, instead, these systems favor the propagation of new faults. In addition, new faults link to the pre-cut fault on the opposite side of the restraining bend with less applied displacement in bends with large θ. The

relationship between applied plate displacement and linkage follows a trend similar to that between plate displacement and the growth of fault I, with less plate displacement required for the linkage of fault I to the opposite side of the restraining bend as θ increases.

The relationship between applied plate displacement and fault abandonment does not trend with θ (open circles on Figure 7). We do observe that fault abandonment often occurs in conjunction with (1) the linkage of a new fault to the pre-cut fault on the opposite side of the bend, as in the θ = 20° and 25° experiments after ~48-50mm of applied plate displacement, or (2) the propagation of a new fault, as in θ = 20° bend at 50 and 73 mm of plate displacement and in the θ = 30° bend at 60-65 mm of plate displacement. However, within the duration of these experiments, no fault is abandoned in the 10° or 15° bend, even after the new faults link to the pre-cut fault across the bend. Several new faults are quickly abandoned in the θ = 15° and 25° bends.

In certain instances, abandoned faults are reactivated. This occurs in the θ = 25° experiment, where a small fault that forms at an applied plate displacement of 22 mm is later reactivated when another new, oblique-slip fault links to it. This is best view in the video included in the supplemental materials, but is also shown in Figure 6.

1.4.2 Strike-Slip Efficiency

In order to evaluate the mechanical efficiency of the evolving fault systems, we define strike-slip efficiency as the amount of strike-slip along all faults within a restraining bend, divided by the applied plate displacement. We do not include slip measurements along the pre-cut fault segments outside of the bend. By restricting our region of interest to the restraining bend, we focus on the effect of the evolving faults on

the strike-slip efficiency of the system. The only exception to this is for the $\theta = 0°$ experiment, which has no restraining bend. In this experiment, we measure efficiency within a central region of interest along the fault. A strike-slip efficiency of 100 % indicates that the amount of strike-slip along all active faults within the restraining bend equals the applied plate displacement and the system has no off-fault deformation or dip-slip. Deformation within such a system resembles slip between two rigid blocks. A strike-slip efficiency of 0 % indicates that none of the applied strike-slip plate displacement is localized as strike-slip, and the applied strain is taken up by off-fault deformation or dip-slip. We expect bends with small θ to be more strike-slip efficient than bends with large θ, because the faults within low angle restraining bends deviate less from the direction of applied plate displacement and therefore can accommodate more applied displacement as strike-slip.

Indeed, we find that faults within high angle bends ($\theta = 20°$, 25° and 30°) are initially less strike-slip efficient than faults within low angle bends ($\theta = 0°$, 10° and 15°) (Figure 8A). Consequently, faults in restraining bends with high θ initially accommodate less applied displacement as strike-slip. We find that, over the range of plate displacement from 10 mm to 25 mm, strike-slip efficiency increases with θ, demonstrating that θ controls how strain is partitioned in the system. This dependence of strike-slip efficiency on θ also is shown in Figure 8B, in which θ is plotted against the rate of change in strike-slip efficiency before fault I propagates in each experiment.

We define steady strike-slip efficiency as an efficiency of ~80 %, as faults within all the restraining bends achieve this efficiency by the end of the experiment regardless of θ (Figure 8A). After this, the faults within these systems do not significantly increase or

decrease in strike-slip efficiency. Faults within the θ = 0° bend reach 80 % efficiency after 12 mm of plate displacement. When θ > 0°, it controls when the system reaches this efficiency level. Faults within the 10° bend reach 80 % efficiency after 70 mm of plate displacement, whereas faults in the θ = 15° bend reach this point after 55 mm plate displacement, and faults within high angle restraining bends of θ = 20°, 25° and 30° reach this point after only ~30 mm of applied plate displacement, despite being the most inefficient initially. Faults within these high angle bends increase in strike-slip efficiency at a constant rate from 8 mm to 33 mm of plate displacement. In contrast, the θ = 10° and 15° bends increase in efficiency at a faster rate initially, but this rate decreases after 15 mm of applied displacement. Relative to the θ = 10° experiment, the drop in strike-slip efficiency is more pronounced in the θ = 15° experiment and the efficiency of the system actually decreases prior to increasing to 80 % efficiency. Decreases in efficiency also occur in other systems, most notably in the θ = 30° experiment after ~50 mm of applied displacement.

To further study the relationship between fault activity and strike-slip efficiency, we closely examine the θ = 20˚ and 30˚ experiments. The fault systems within these high angle bends continue to improve in strike-slip efficiency until the first new fault propagates, indicated by the stars in Figure 8A. After this point, strike-slip efficiency increases at a slower rate. In addition, in the θ = 30˚ experiment, reaching a steady strike-slip efficiency of ~80 % precedes the linkage of fault I to the right side of the pre-cut fault by ~8 mm of plate displacement. From this observation, we interpret that fault I, and potentially other new faults, link to the pre-cut fault at depth before doing so at the clay surface. The linkage of fault I in the θ = 30˚ experiment allows faults to achieve steady

strike-slip efficiency. However, the linkage of fault II to the pre-cut fault in that same experiment does not produce a noticeable increase in strike-slip efficiency.

However, we do observe small changes in strike-slip efficiency with the propagation, linkage and abandonment of faults even after strike-slip efficiency has reached 80 % (Figure 8A, inset). The relationships between this faulting behavior and efficiency are complex, and this also may be due to activity at depth that precedes what is observed at the surface with PIV. The inset in Figure 8A highlights the evolution of strike-slip efficiency for faults in the $\theta = 20^{\circ}$ and 30° bends late in these experiments. Just after the linkage of fault I to the opposite side of the $\theta = 20^{\circ}$ restraining bend at 48 mm of applied displacement, fault II begins to propagate and the strike-slip efficiency increases by ~5 % (Figure 8A, inset). Then, the abandonment of fault I and the propagation of fault III coincide with another 5 % increase in efficiency (Figure 8A, inset). For the $\theta = 20^{\circ}$ experiment, the abandonment of fault I is nearly simultaneous with the initiation of fault III at 73 mm of plate displacement, which may obscure the expected decrease in strike-slip efficiency with fault abandonment. (Figure 8A, inset). However, in the $\theta = 30^{\circ}$ bend, propagation of fault III occurs at a local minimum of strike-slip efficiency at 78 % and an increase in efficiency follows. The linkages of faults II and III increase the strike-slip efficiency again by about 10 % (Figure 8A, inset). Thus, we observe that the reorganization of active faults within the restraining bends can cause small changes to a relatively steady strike-slip efficiency, but the details in the relationships between fault propagation, linkage and efficiency are difficult to resolve with the surface data alone. Overall, the reorganization of active faults within the experimental bends maintains

strike-slip efficiency at a constant level; abandonment, propagation and linkage of faults regulate the strike-slip behavior within the restraining bend fault system.

We also observe that very different active fault systems can have the same strike-slip efficiency. In Figure 8C, we show the fault systems from the $\theta = 15°$ and 30° restraining bends after 28 mm of applied plate displacement. Both systems are 60% strike-slip efficient, but the active fault systems differ in geometry and faulting style. New, oblique-slip faults within the $\theta = 30°$ bend continue to propagate toward the opposite sides of the bend. Slip in the $\theta = 15°$ bend is mainly strike-slip along the pre-cut fault through the bend. Experimental restraining bends can accommodate the same amount of applied plate displacement as strike-slip and yet maintain very different active fault behavior (Figure 8C).

1.4.3 Convergence controls on fault growth

As demonstrated in Figure 7 and discussed previously, new faults propagate after less plate displacement in high angle bends compared to low angle bends. We expected that the timing of new fault propagation would relate to some threshold of strike-slip efficiency. However, in the $\theta = 30°$ bend, the growth of the fault I occurs at a strike-slip efficiency of ~10 % and this growth increases the efficiency of the system (Figure 9). In contrast, the pre-cut fault in the $\theta = 10°$ bend has a strike-slip efficiency of nearly 80 % when a new fault propagates, suggesting the new fault is not required to increase the efficiency of the restraining bend. Figure 8 summarizes these data for all experiments, showing that new faults grow at various strike-slip efficiencies in different fault systems.

Instead, we find that a threshold of accumulated convergence at which fault I propagates, averaging 5.3 ± 0.3 mm. The threshold accumulated convergence value is

independent of θ. (Figure 9; Table 1). We calculate the accumulated convergence when fault I propagates as the tangent of θ. Propagation occurs after less applied plate displacement when θ is large because these systems accumulate more convergence with less applied plate displacement. The opposite is true when θ is small: more plate displacement is required for the system to reach threshold convergence and for a new fault to grow.

Convergence is accommodated within restraining bends by oblique-slip along new faults. To measure the dip of these faults and evaluate if fault dip varies with θ, we reverse the claybox motor after completion of the θ = 13˚ and θ = 25˚ experiment unslip the faults, and take 3D laser scans of the exposed fault surfaces. We observe no differences in the dips of new faults in low and high θ bends. However, dip varies along each individual new fault surface. In general, a new fault dips 60˚ - 70˚ near its initiation point at a kink in the bend, where the fault is connected to the vertical, pre-cut fault, then rotates to dip 35˚ - 45˚ far from its initiation point. This observation agrees with two dimensional work minimization numerical models of mechanically efficient faults (Cooke and Murphy, 2004). Additionally, the pre-cut fault segments within the bend rotate up to 10˚ from a pre-cut dip of 90˚. All faults dip into the uplift.

While total convergence within the system corresponds to the timing of new fault propagation, we investigate the location of convergence within the system to test if faults grow in areas of high convergence accommodation within the fault system. Using PIV, we are able to locate regions of high incremental convergence prior to fault propagation, calculated as the magnitude of the surface displacement perpendicular to the applied plate displacement direction. We find that the locations of new faults correspond to regions of

high incremental convergence on the clay surface within the restraining bend (Figure 10). For instance, in the $\theta = 10^{\circ}$ bend, the incremental convergence is high within the restraining bend early, near the location of the propagation of fault I (Figure 10A and B). In addition, in the $\theta = 30^{\circ}$ bend, incremental convergence is high in the propagation paths of both faults I and II (Figure 10C and D). Thus we find that θ dictates where convergence accumulates within the bend and the resulting pattern of fault system evolution.

1.5 Discussion

1.5.1 Slip rates along the Dead Sea Fault, Lebanon

A $15^{\circ} \leq \theta \leq 20^{\circ}$ restraining bend along the Dead Sea transform fault, bisecting Lebanon, is proposed to have been strain partitioned throughout the Cenozoic (Gomez et al., 2007). The approximately vertical segment of the Dead Sea Fault that within the restraining bend, the Yammouneh Fault, accommodates NNE-SSW left-lateral strike-slip. Two oblique-slip faults sub-parallel to the Yammouneh Fault within the bend, the Sergahaya and Roum faults, host much slower slip rates. The strike-slip rate along the Yammouneh is estimated to be 5.0 ±1.1 mm/year, a rate obtained by dating an offset alluvial fan (Gomez et al., 2007). This accommodates all of the the Arabian Plate motion, measured at 4.8 mm/year relative to the Sinai Plate of along a vector oriented at N10˚W (Reilinger et al., 2006). When translated to be parallel to the Yammouneh Fault, strike-slip portion of the plate rate is even lower, at 3.8 mm/year (Gomez et al., 2007). Even at the minimum estimated strike-slip rate, and without accounting for slip along the Segahaya and Roum faults, the slip rate of the Yammouneh Fault exceeds the plate rate as currently calculated. Gomez et al. (2007) explains this discrepancy by stating the

geologic slip rate may be overestimated. Another explanation is that the plate rate has slowed over time.

The analog models provide alternative explanations for the presence of this high slip rate. One possibility is that the strike-slip rates along the faults near this restraining bend vary in time and space, even while the plate rate has remained constant. Under this scenario, the geologic slip rate estimated for the Yammouneh Fault may reflect a faster rate from the past, or be a local phenomenon sustained even while the average slip rate for the entire fault may be slower. This is observed along the claybox faults, which accommodate strike-slip at variable rates over the course of an experiment. In Figure 11, we show how strike-slip efficiency, the strike-slip rate normalized by the applied plate rate, changes along y-transects in the $\theta = 15^{\circ}$ and $\theta = 30^{\circ}$ restraining bends at three snapshots during the experiments; fault maps for these experiments with the y-transect lines are shown in Figure 4. Using these plots, we are able to track increasing strike-slip efficiency as discrete faults develop early in the experiments. In Figure 11A, this is observed within the $\theta = 15^{\circ}$ restraining bend near y = 17 cm and y = 18.5 cm. The high efficiency near y = 18.5 cm is along the pre-cut fault segment within the bend, similar in geometry to the Yammouneh Fault. Here, strike-slip efficiency increases from ~20 % to 30 % between 10 mm and 50 mm of plate displacement, then increases again to 22 % by 85 mm of plate displacement. The increasing efficiency near y = 17 cm is along fault I, the first new, oblique-slip fault to grow. At fault I, or, for instance, the Sergahaya Fault, strike-slip efficiency increases from 10 % to 18 % between 10 mm and 50 mm of plate displacement, then decreases to 22 % by 85 mm of plate displacement. The strike-slip efficiency of the entire fault system by this time is constant at ~80 %. This suggests that

this local increases/decreases in efficiency are balanced by local decreases/increases at other locations. Efficiency changes likely have occurred in locations not crossed by the transect, as well. The combination of such local variations across the entire restraining bend likely contribute to the noise of the strike-slip efficiency data for the entire system shown in Figure 8A.

Similar trends are observed in the $\theta = 30^{\circ}$ experiment, where the strike-slip efficiency of fault I at y = 20.5 cm and fault II at y = 25 cm change over time (Figure 11B). Near fault I, strike-slip efficiency increases from 20 % to 60 % from 10 mm to 50 mm of plate displacement, then decreases to 56 % by 85 mm of plate displacement. Near fault II, strike-slip efficiency increases from ~70 % to 85 % between 10 mm and 50 mm of plate displacement, then increases by another ~2 % by 85 mm of plate displacement.

From these results, we infer that the slip rate estimate along the Yammouneh Fault may be from data collected at particularly fast slipping portions of the fault. Field estimates of an average strike-slip rate for this fault may be complicated further by the fact that rates likely change at a particularly location over time. Such behavior should be considered when strike-slip rates of crustal systems are estimated geologically.

1.5.2 Topography along the Denali Fault, Alaska

Figure 12 also shows that the uplifted regions within both restraining bends behave as rigid blocks, moving at the same strike-slip efficiency as fault I in both experiments. The decrease in strike-slip efficiency along fault I between 50 and 85 mm of applied plate displacement in both experiments is apparent from the strike-slip efficiency recorded across blocks.

These blocks are also actively deforming and uplifting during deformation. To further explore the development of topography within the restraining bend, we compare the topographic relief produced by the experiment with $\theta = 25^{\circ}$ and an additional experiment with $\theta = 13^{\circ}$, which reflects the geometry of a restraining bend along the Denali fault in Alaska. The uplift resulting from deformation near the $\theta = 25^{\circ}$ restraining bend is symmetric, bounded by two new oblique-slip faults on opposite sides of the pre-cut segment of the fault within the bend (Figure 12A). In the $\theta = 13^{\circ}$ experiment, a new fault and the pre-cut fault segment within the bend bound the area of uplift (Figure 12B). The pre-cut fault marks the edge of a steep topographic gradient, while the new fault marks the edge of more gradually changing topography. The topography within the restraining bend therefore is asymmetric. This asymmetry is similar to that observed along the Denali bend, where topography is higher on the south side of the restraining bend than to the north (Figure 12C). The topographic gradient from A to A' across the Denali bend from north to south and across the claybox demonstrate this similarity (Figure 12D). Though we do not incorporate erosion into the analog models, the resultant topography, and its gradient in particular, is remarkably similar between this crustal example and the claybox.

1.5.3 Fault evolution with the San Gorgonio Knot, California

The San Gorgonio Knot is a restraining bend along the southern San Andreas Fault in California (USA). Work by Matti et al. (1992) and Matti and Morton (1993) suggests multiple stages of fault evolution in this region over the last 500 kya. Before 500 kya, the Mission Creek segment of the San Andreas fault was active as a thrust fault at a compressional jog in an predominantly strike-slip system (Figure 13). Together, these

three segments formed a restraining bend with θ = 25°. Between 500 and 120 kya, the strike-slip Mill Creek segment replaced the Mission Creek segment as an active segment within the bend. The San Gorgonio Pass thrust fault also may have been active at this time. Between 120 kya and present day, the eastern portion of the Mill Creek segment was abandoned in favor of a complex set of faults including the sub-parallel, north-dipping Banning, Garnet Hill and San Gorgonio Pass thrust faults. These three faults all developed outboard of the region of uplift. Numerical modeling by Cooke and Dair (2011) shows an increase in mechanical efficiency, a measurement of the energy of the system, between the systems of faults active at 500 kya and between 500 and 120 kya. Recent work by Fattaruso et al (in review) show an additional increase in mechanical efficiency due to the fault structural changes from 120 kya to the present. This suggests that the system has evolved toward higher efficiency over geologic time, as is seen in the analog experiments.

In addition, the transition from strike-slip faulting within the bend along the Mill Creek segment between 500 and 120 kya to the development of the currently active Banning, Garnet Hill and San Gorgonio Pass thrust faults is similar to the fault development captured in the θ = 25° restraining bend experiment, shown in Figure 7. In this experiment, the pre-cut fault within the bend begins to slip initially (Figure 7, 10mm plate displacement). However, soon after strike-slip localizes on the restraining bend segment, a new, oblique-slip fault has developed on one side of the bend (fault I, Figure 7). By the end of the experiment, slip through the bend is accommodated by two new oblique slip faults on either side of the bend, with the restraining segment abandoned at 47 mm of plate displacement (Figure 7). At ~35 mm of applied plate, the strike-slip

efficiency of this fault system already has reached ~80 % (Figure 7). Any changes to the fault system after this time serve only to maintain this efficiency level, including the development of fault II and eventual propagation of fault IV.

Despite this global consistency in strike-slip efficiency, we find that spatial and temporal changes in efficiency continue during large structural changes to the fault system. In the $\theta = 25^{\circ}$ restraining bend, at 57 mm of plate displacement, the lower left corner of the restraining bend is marked by low strike-slip efficiency; no fault is active on the surface of the clay at this point (Figures 14A and B). However, fault III has propagates into the region by 74 mm of plate displacement, and the region of previously low strike-slip efficiency shrinks (Figures 14C and D). At this point, the region between faults I and III remains slightly less efficient than the rest of the restraining bend (Figure 14D), until fault IV grows outboard of fault I at 84 mm plate displacement (Figures 14E and F). Thus, fault propagation and linkage may serve to locally increase strike-slip efficiency, even while the global efficiency remains relatively constant.

At 84 mm plate displacement, the strike-slip efficiency of the block within the bend decreases (Figures 14E and F). Because the strike-slip efficiency of the system is relatively constant at ~80 % by this time, this must be compensated by higher strike-slip efficiency elsewhere. In fact, the strike-slip efficiency of the clay on the opposite side of the bend appears to have increased by this time. It is moving at a rate approaching the applied plate rate, with a strike-slip efficiency of ~100 %. This is likely related to efficient slip along fault II and suggests that this fault is the dominant slip surface for the system.

All of the claybox experiments reach a steady strike-slip efficiency of ~80 % and this reflects observations of crustal systems. From examinations of fold propagation and paleomagnetic rotation, Titus et al. (2007) find that 80 % of the relative plate motion is accommodated by displacement along the Rinconada fault in California, USA, with 20 % of the plate motion accommodated off of the fault. Shelef and Oskin (2010) observe that 0-25 % of plate motions in the Eastern California Shear Zone are accommodated by off-fault deformation, measured as distributed displacement and modification of rock properties due to block rotation and fragmentation in zones adjacent to main faults. This leaves 75 – 100 % of plate motion to be accommodated by slip along faults.

1.5.4 Evolution of restraining bend aspect ratios

Wakabayashi et al. (2004) report on field studies of the spatial and temporal evolution of crustal restraining bends. They observe propagation and abandonment of faults only on one side of bends. We show that this asymmetry depends on θ and observe similar evolution to the systems studied by Wakabayashi et al. (2004) for experiments with low θ. However, we find that the high θ experiments exhibit more symmetric fault growth patterns, with new faults initiating from the kinks on both side of the restraining bend.

Wakabayashi et al. (2004) also suggest restraining bends will migrate over time as the restraining bend contracts. In the Dead Sea transform system, Gomez et al. (2007) estimates up to 17 % contraction within the restraining bend over the Cenozoic, meaning the bend itself has shortened and, according to Wakabayashi et al., (2004), should only migrate along strike. Other workers have postulated that as restraining bends evolve, they lengthen more than widen as imbricate faults form bounding the uplifted region (Cunningham 2007; Cunningham and Mann 2007; Swanson 2005). The analog models

presented here aid understanding of how restraining bends change in shape over time. Initially in the experiments, before the propagation of the first new fault, we observe a process of shortening while convergence accumulates within the bend (Table 2). By the end of the experiment, we observe the bends lengthening, as new oblique-slip faults propagate from at least one kink in all experiments and grow toward the opposite side of the bend (Table 2).

To quantify the changes in the dimensions of the experimental restraining bends, we measure aspect ratio as the length of the restraining bend divided by the width of the restraining bend. The length is initially measured as the lateral distance between the two pre-cut kinks, parallel to the pre-cut fault outside of the restraining bend. The final length is measured between the tips of the active faults bounding the uplift, also parallel to the pre-cut fault outside of the restraining bend. These active faults may include new, oblique-slip faults, on one or both sides of the bend. The initial width is equal at 5 cm for all experiments in this study. The final width of the bend is the width of the uplift bound by active faults perpendicular to the pre-cut fault outside of the restraining bend.

The results corroborate observations of both significant contraction within the restraining bend while convergence accumulates, followed by lengthening of the bend (Table 2). These processes are directly related to fault growth. Once the threshold convergence is reached within each restraining bend, a new oblique-slip fault propagates. These faults eventually both lengthen and widen the bend. Restraining bends with $\theta > 15^{\circ}$ tend to lengthen more than they widen, while the $\theta = 15^{\circ}$ restraining bend changes in both dimension equally and the $\theta = 10^{\circ}$ restraining bend widens more than it lengthens. The large difference in the percent changes of length between low and high angles is because

high angle bends propagate two new faults throughout the experiment, extending the bend on either side of the pre-cut fault, while low angle bends only propagate one new fault, on one side of the restraining bend.

1.6 Conclusions

We present analog models of restraining bends with θ ranging from 0˚ to 30˚. New faults propagate at less applied plate displacement in experiments with high θ relative to those with low θ. In addition, the pre-cut faults within restraining bends slip throughout the experiment, whereas that same fault is abandoned with small amounts of plate displacement in high θ experiments. Despite these differences, the new first fault propagates at a threshold convergence in all experiments, regardless of θ. The pre-cut fault is abandoned in high angle bends with less applied plate displacement compared to low angle restraining bends. The first fault propagates at a threshold convergence in all restraining bends, regardless of θ. Strike-slip efficiency does not control when the first fault propagates. Strike-slip efficiency of the fault system does not control when this first fault propagates.

When a new fault propagate, strike-slip efficiency decreases for a time, likely indicating that more applied displacement is being accommodated as convergence along the new oblique-slip fault. However, the strike-slip efficiency generally recovers and continues to increase follow this temporary decrease. All experiments attain a steady strike-slip efficiency of 80% before follow the end of the experiment. Propagation of new faults after this steady strike-slip efficiency is reached appear to only maintain the efficiency. This efficiency of 80% reflects the strike-slip efficiency estimated for crustal

systems. Despite these similar final strike-slip efficiencies, all experiments produce restraining bends with different final fault geometries, as well as varying evolution patterns when new faults propagate, link and abandon in acquiring this final fault geometry.

Wet kaolin restraining bends provide a reliable analog to crustal systems with respect to fault and mechanical evolution, as well as topography. Asymmetric topographic gradient and asymmetric fault growth observed in the Denali restraining bend, as well as a complex evolution of system wide strike-slip efficiency within the San Gorgonio Knot, are all mimicked well in our models.

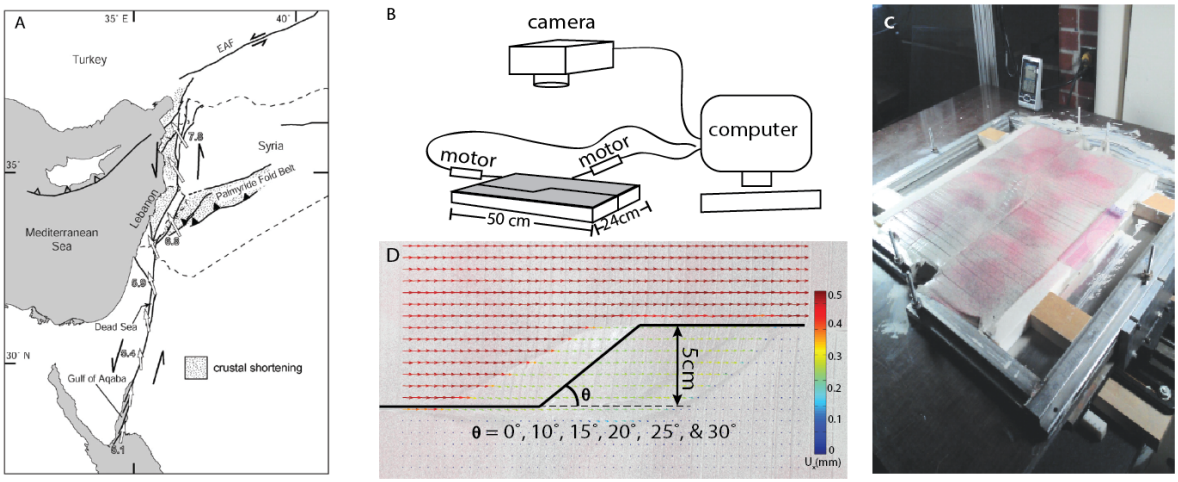

Figure 1.1 Experimental set-up and motivation:

A) Modified fault map after *Gomez et al.* [2007]. Map of the Dead Sea restraining bend located within Lebanon and surrounding countries. Mount Lebanon range is uplifted within the restraining bend west of the Dead Sea fault. RF-Roum Fault, YF-Yammouneh Fault, SF-Serghaya Fault. B) Cartoon of claybox set-up, depicting x- and y-motors and an overhead camera controlled by a computer. C) Restraining bend claybox experiment. We sprinkle the kaolin surface with red and black sand to provide contrasting pixels for PIV tracking. Ruler is 15 cm long. D) Image from claybox experiment overlain with PIV plate-parallel displacement field. Gradients reveal active faults at 40 mm plate displacement. A schematic initial restraining bend is overprinted in black showing the angles, θ, used in this study.

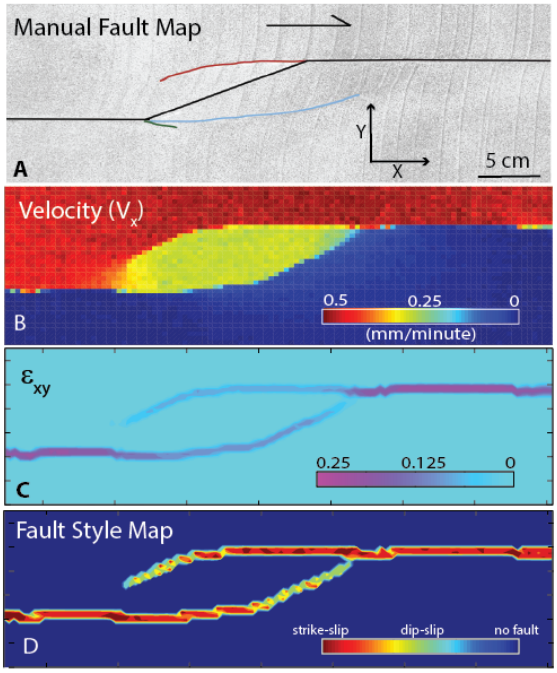

Figure 1.2 Qualitative and quantitative map comparison

Four fault maps of θ = 30˚ experiment at 40mm plate displacement. A) Manual mapping (black faults indicate pre-cut faults, red, blue and green faults indicate newly propagated faults). B) Strike-slip velocity map between successive photos. C) Shear strain map. D) Fault style map. Red indicates plate-parallel motion on faults parallel to the x-direction (motor displacement) and teal indicates plate-normal motion along that segment. Obliquely oriented faults from θ = 10˚ to θ =30˚ (the range tested) with pure plate-parallel (strike-slip) would appear orange so that yellow indicates oblique-slip. Map A provides a general fault map, but maps B, C and D provide more quantitative information about the fault evolution within the bends.

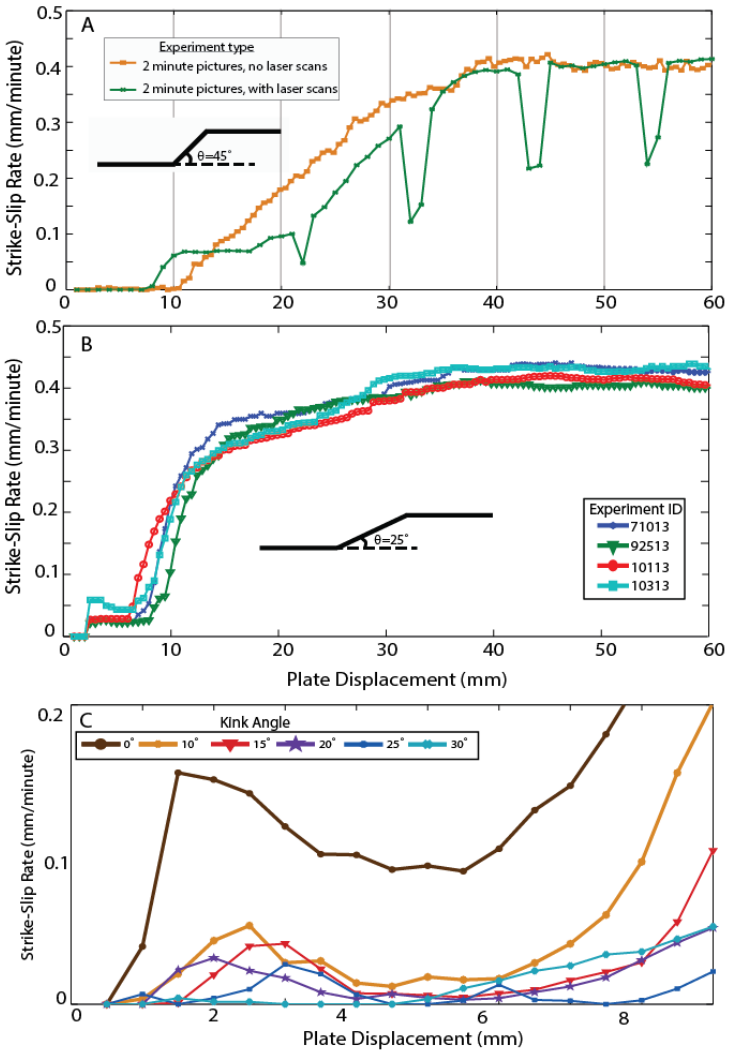

Figure 1.3 Method proof of concept

A (top): Strike-slip rates of two θ = 45˚ experiments with different data collection methods. The green curve describes PIV measured plate-parallel slip using two minute picture intervals (1mm plate displacement/image). This experiment was also arrested every 10 mm of plate displacement to collect laser scans. The brown curve shows slip rates of an experiment with only PIV images (no stoppages during the experiment). B (middle): Strike-slip rates of four θ = 25˚ experiments to test experiment repeatability. Experiments are repeatable in plate-parallel slip. The most variability is in the initial plate displacement. Legend describes different experiment names but data plotted are from the same experimental set up. C) Initial strike-slip rates of all bends. Slip rates increases, decreases, then increases again in all experiments except for θ = 30˚ experiment.

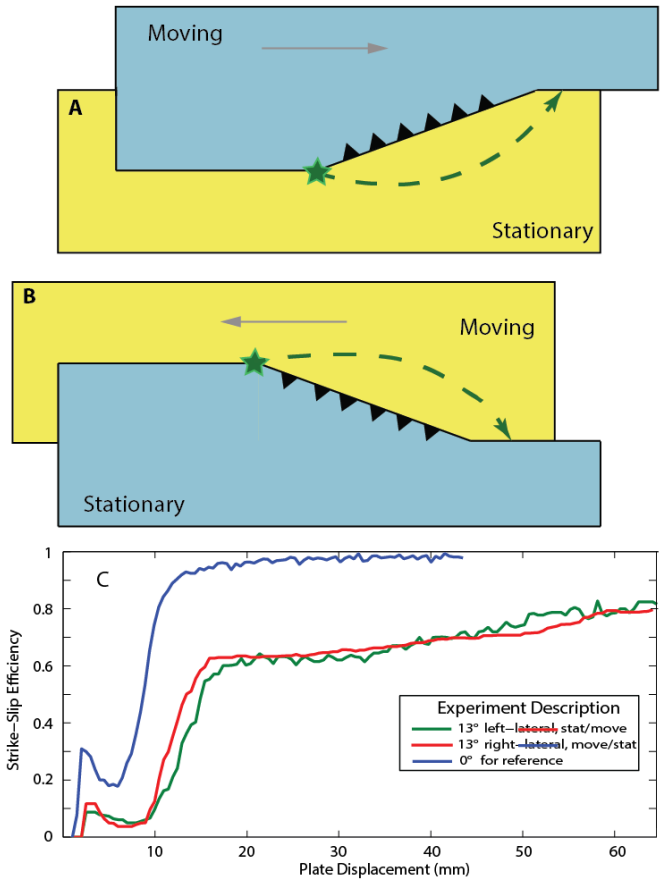

Figure 1.4 Location of first fault initiation

Oblique-slip faults initiate over the underthrust plate regardless of whether this plate is moving or stationary. A) Map view of right-lateral restraining bend with moving plate overriding the stationary plate in the standard experimental set up. B) Alternative experimental set up with left-lateral restraining bend using the stationary plate as the overriding plate. The first oblique-slip fault initiates in the same place (green star) and propagates around the restraining bend over the underthrust plate (green dashed arrow). C) The faults behave similarly, as observed in the near congruence in strike-slip efficiency. The noise in the data for the moving plate under the stationary plate experiment reflect the relative difficulty of the motor to advance the moving plate in this configuration.

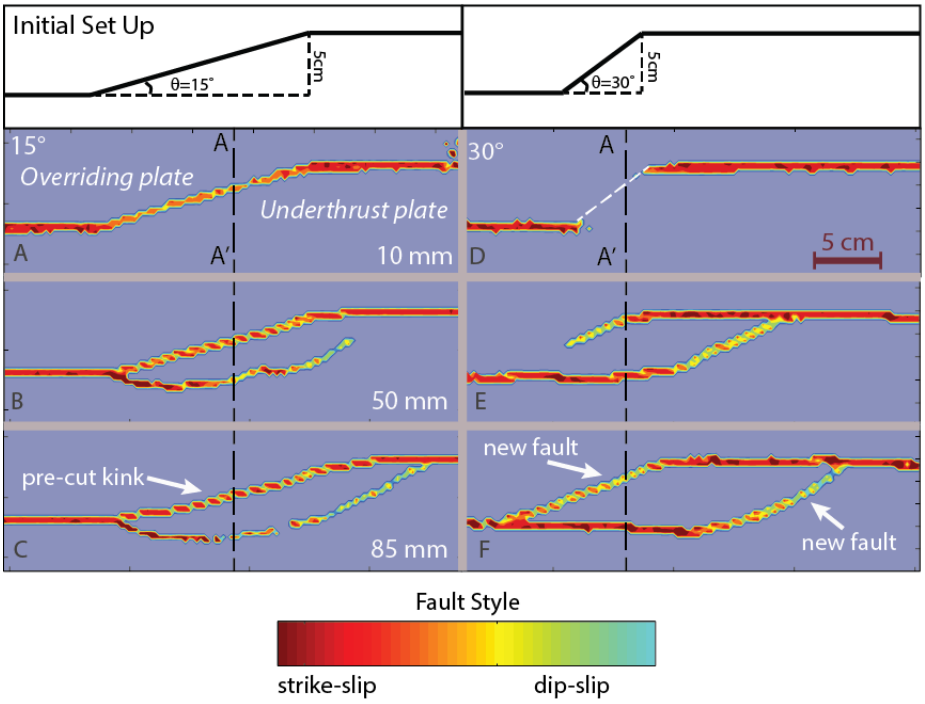

Figure 1.5 Fault style maps comparing θ=15˚ and θ=30˚

Fault style maps show the fault evolution within the experiments with θ = 15˚ and 30˚ representing low and high angle bends. As plate displacement increases, oblique-slip faults propagate, accommodate plate-parallel slip, and link to pre-existing faults (B and E). Low angle bends slip along the pre-cut restraining fault segment for the entire experiment (A-C). New faults propagate at a high angle away from the pre-cut fault in low θ bend and at a low angle in the high θ bends (gray arrows in B and E). The pre-cut fault in the θ = 30˚ experiment is represented by a white dashed line in map D. Oblique-slip faults propagate on both sides of the pre-cut restraining bend segment in the high angle experiments; in low angle experiments, oblique-slip faults propagate only above the underthrust plate. Dashed lines of section (A-A') are presented in Figure 1.14.

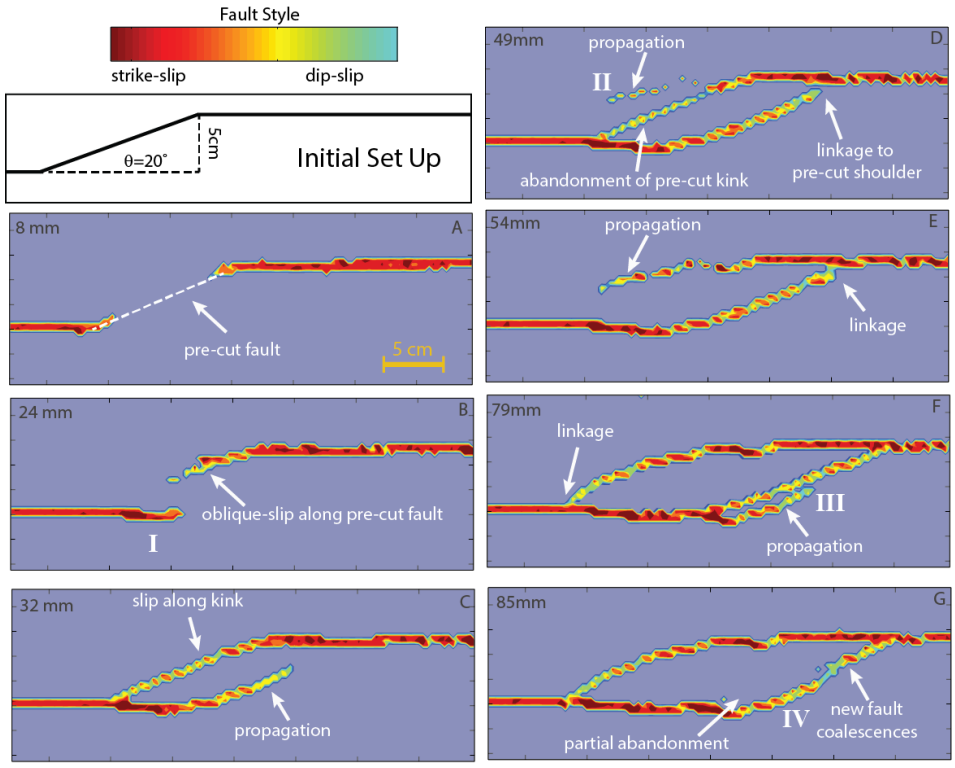

Figure 1.6 In depth fault evolution of θ=20˚

Detailed fault evolution of θ = 20˚ restraining bend, showing initiation, propagation, linkage and abandonment. Faults discussed in the text are labeled with Roman numerals I-IV in order of initiation, which is systematic in all experiments.

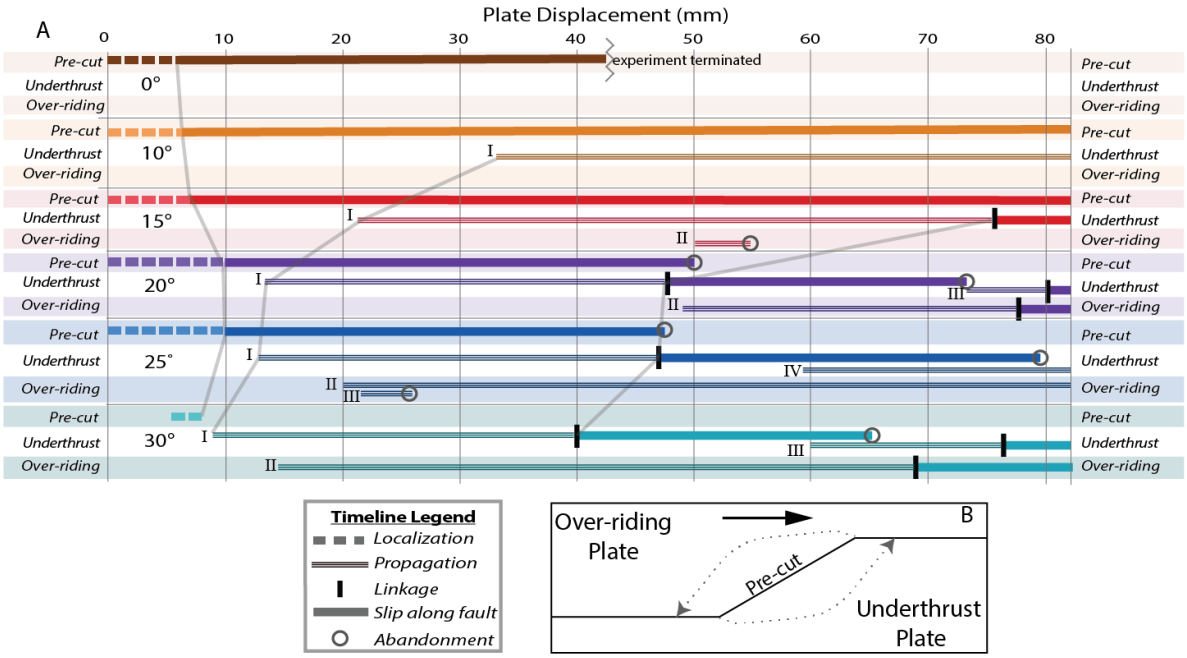

Figure 1.7 Fault evolution timeline

Graphical representation of fault evolution. The timeline highlights localization, propagation, linkage and slip for the pre-cut bend segment and faults propagating above the underthrust and overriding plates. Each horizontal line represents the activity of one fault within the experiment. Stacked lines indicate the time which multiple faults are active. The different experiments are delineated with different color lines in different rows of the timeline. Faults within each experiment are characterized by location of fault initiation. Roman numerals indicate fault number based on growth order for each experiment, as in Figure 1.6. B) Schematic map showing plate relationships.

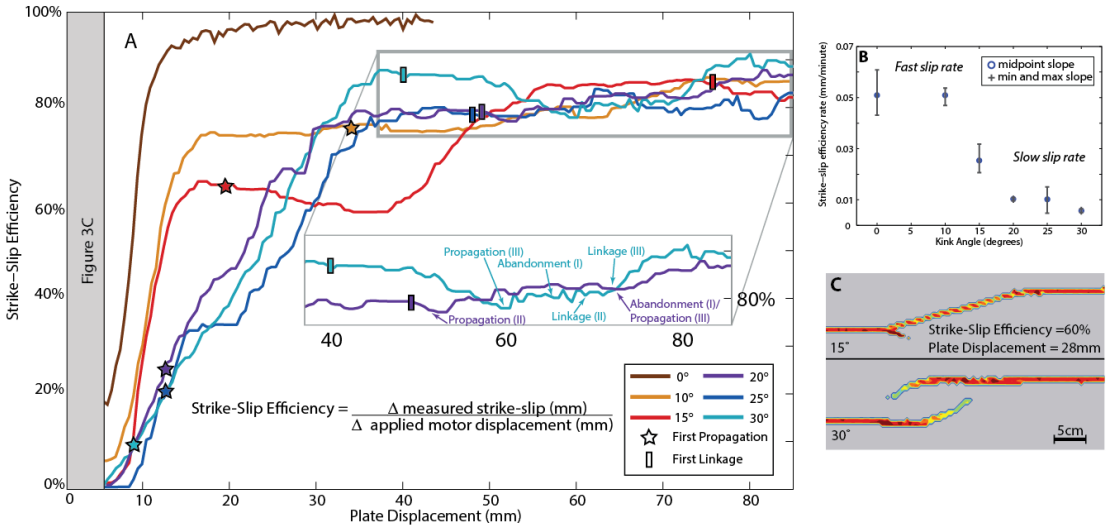

Figure 1.8 Strike-slip efficiency

A) Strike-slip efficiency versus applied plate displacement. Strike-slip efficiency is the ratio of measured strike-slip rate on all faults within the restraining bend to applied plate velocity. Data is smoothed using a moving median method to reduce noise from the stepper motor. Inset shows only $\theta = 20^{\circ}$ and $\theta = 30^{\circ}$ experiments for detailed analysis of efficiency as related to the structural evolution of the bend. B) Strike-slip efficiency rate decreases as θ increases, showing that high angle restraining bends partition deformation as strike-slip along faults slower than low angle restraining bends. Partitioning rate is the initial slope of the strike-slip efficiency plot, and bars show the range of slope before the propagation of the first fault. C) Two fault style maps showing $\theta = 15^{\circ}$ and $\theta = 30^{\circ}$ at 28mm plate displacement. Faults within both restraining bends are 60% strike-slip efficient, but the active fault configurations are very different.

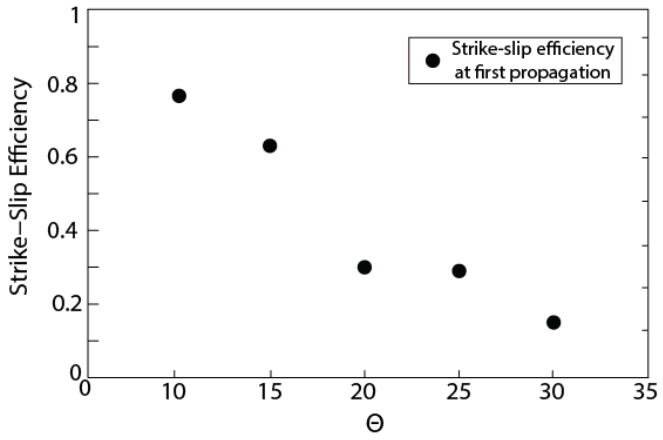

Figure 1.9Efficiency at first propagation

Strike-slip efficiency at the time of first fault propagation for all θ. First fault propagation does not depend on strike-slip efficiency, and is instead controlled by accumulated convergence.

Theta	10	15	20	25	30
Strike-Slip Displacement (mm)	31	21	13	12	9
Accumulated Convergence (mm)	5.5	5.6	4.7	5.6	5.2
Convergence : Strike-Slip	0.18	0.27	0.36	0.47	0.58

Table 1.1 Convergence at first fault propagation

Convergence at first fault propagation calculations for various θ.

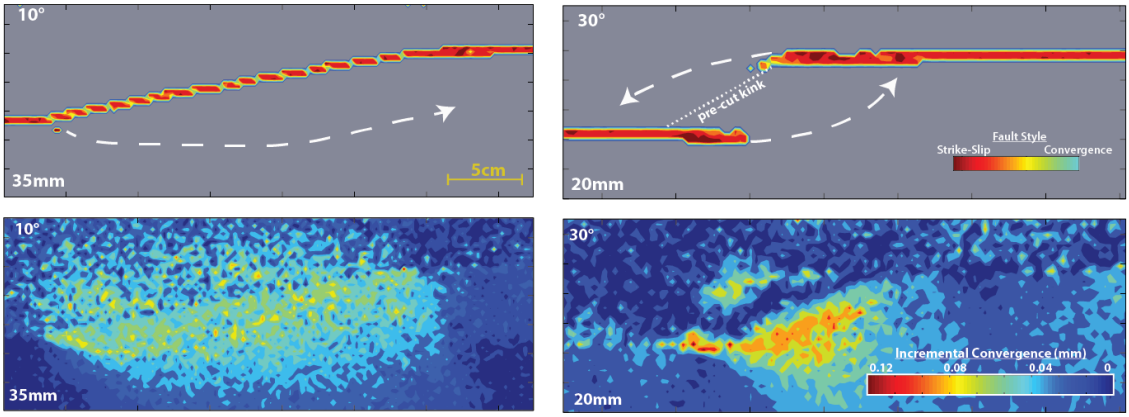

Figure 1.10 Convergence maps of θ=10˚ and θ=30˚

Top row: Fault style maps of θ=10˚ and θ=30˚ at 35 and 20mm plate displacement. Bottom row: Incremental convergence of experiments. Propagation of incipient faults indicated with white dashed arrows. Convergence accumulates in the restraining bend in both low and high angle bends. Low angle bends accumulate convergence between the pre-cut fault and incipient oblique-slip fault; high angle bends accumulate convergence in the propagation path of the incipient oblique-slip faults.

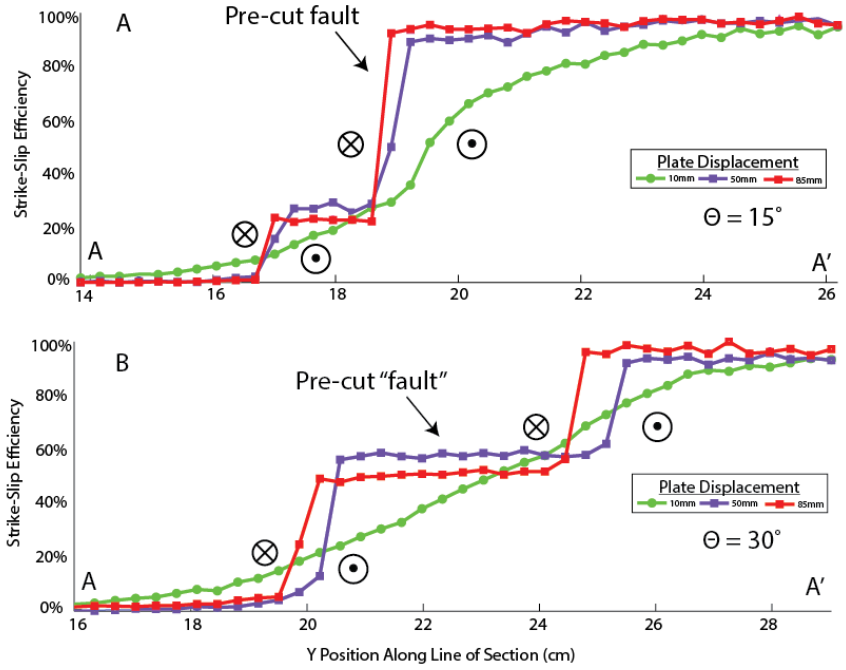

Figure 1.11 Strike-slip efficiency transects of θ=15˚ and θ=30˚

Strike-slip efficiency transect across θ=15˚ (A) and θ=30˚ (B) bends. Transect locations are show on Figure 5 along with fault maps of 10, 50 and 85mm plate displacement. Fault slip sense symbols delineate where faults are active in plate-parallel slip.

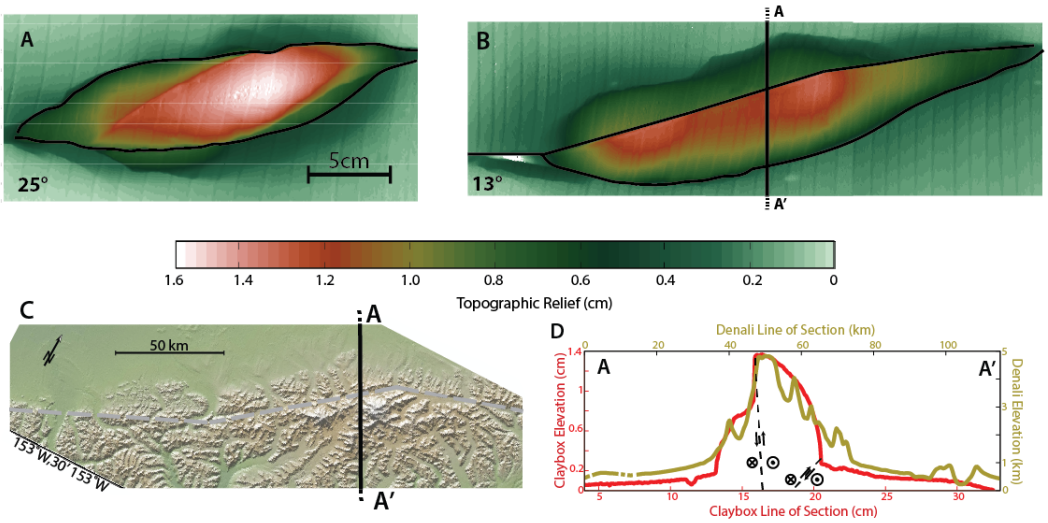

Figure 1.12 Topographic comparison between θ=13˚ and Denali

Top row: 3D laser scans collected after 85mm of plate displacement provide topography accumulated throughout an experiment from θ = 25˚ (A) and θ = 13˚ (B). C) Shaded relief map of simplified Denali Fault trace (Alaska) (dashed gray line). D) Topographic profile along lines of section A-A' from B (claybox) and C (crust).

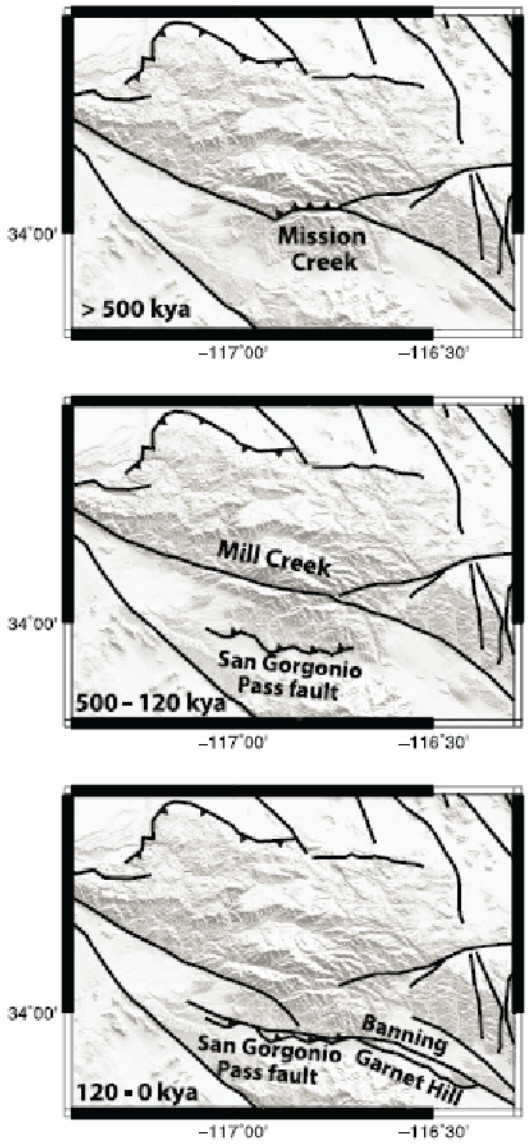

Figure 1.13 San Gorgonio Pass fault evolution

Figure 2 from Cooke and Dair 2011. Maps showing the evolution of fault activity at the San Gorgonio Pass as proposed by Mattie et al. (1992) and Matti and Mortion (1993). Time steps are labeled in lower left corner of each map. The San Gorgonio Pass appears to gain complexity over geologic time, as opposed to achieving an efficient, simpler fault geometry.

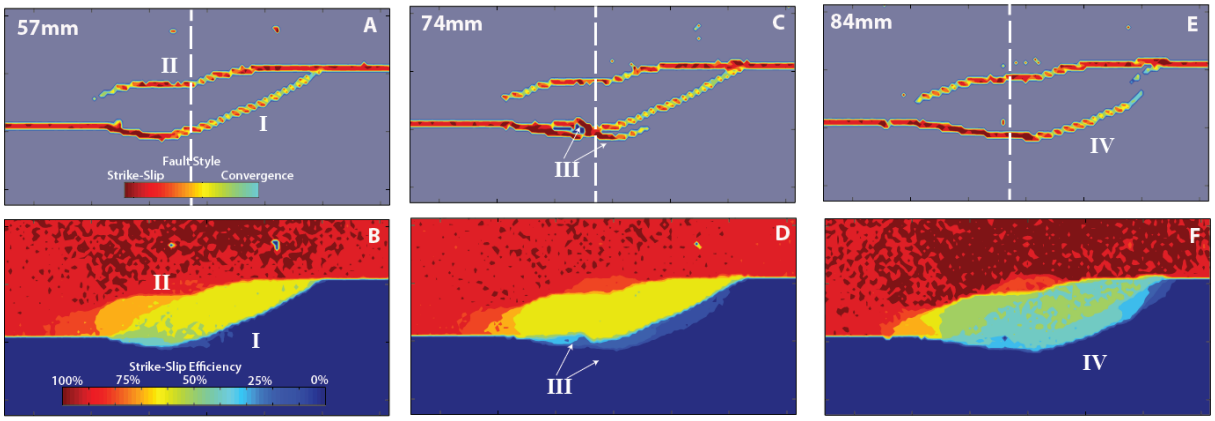

Figure 1.14 Fault maps compared to strike-slip efficiency maps of θ=25˚

Figure 2 from Cooke and Dair 2011. Maps showing the evolution of fault activity at the San Gorgonio Pass as proposed by Mattie et al. (1992) and Matti and Mortion (1993). Time steps are labeled in lower left corner of each map. The San Gorgonio Pass appears to gain complexity over geologic time, as opposed to achieving an efficient, simpler fault geometry.

θ	Initial Length (cm)	Final Length (cm)	Initial Width (cm)	Final Width (cm)	% Δ, Length	% Δ, Width	Initial Aspect Ratio	Final Aspect Ratio	Length at first prop (cm)	First Prop %Δ, Length
10°	28.4	29.9	5.0	5.6	5%	11%	5.7	5.3	27.4	-3%
15°	18.7	26.3	5.0	6.65	29%	25%	3.7	3.9	18.1	-3%
20°	13.7	26.4	5.0	6.2	48%	19%	2.7	4.3	12.5	-9%
25°	10.7	25.04	5.0	6.65	57%	25%	2.1	3.8	9.4	-12%
30°	8.7	28.9	5.0	6.3	70%	21%	1.7	4.6	8.2	-5%

Table 1.2 Aspect ratio of restraining bends

Length, width and aspect ratio of experimental restraining bends at first fault propagation and final plate displacement.

1.7 References

Ackerman, R.V., R.W. Schlische, and M. O. Withjack. "The Geometric and Statistical Evolution of Normal Fault Systems: An Experimental Study of the Effects of Mechanical Layer Thickness on Scaling Laws." *Journal of Structural Geology*, 23 (2001): 1803-819.

Adam, J., J. L. Urai, B. Wieneke, K. Pfeiffer, N. Kukowski, J. Lohrmann, S. Hoth, W. Van Der Zee, and J. Schmatz. "Shear Localisation and Strain Distribution during Tectonic Faulting—new Insights from Granular-flow Experiments and High-resolution Optical Image Correlation Techniques." *Journal of Structural Geology* 27.2 (2005): 283-301.

Adrian, R. J., and J.Westerweel. *Particle Image Velocimetry*. New York: Cambridge UP, 2011.

Cadell, H.M. 1889. Experiment researches in mountain building. *Transactions of the Royal Society of Edinburg*, 1, 339-343.

Cloos, H. (1928), Experimente zur inneren Tektonik, Zen. Min., Geol. Pal., 1928B, 609–621.

Cooke, M.K. and L.C. Dair (2011), Simulating the recent evolution of the southern big bend of the San Andreas fault, Southern California, *Journal of Geophysical Research*, 116.

Cooke, M. L., M.T. Schottenfeld, S.W. Buchanan (2013), Evolution of fault efficiency at restraining bends within wet kaolin analog experiments, *Journal of Structural Geology*, 51, 180-192.

Cooke, M. L., and N. J. van der Elst (2012), Rheologic testing of wet kaolin reveals frictional and bi-viscous behavior typical of crustal materials, Geophys. Res. Lett., 39.

Cooke, M.L. and S. Murphy (2004), Assessing the work budge and efficiency of fault systems using mechanical models, J. Geophys. Res., 109.

Cunningham, W.D., and P. Mann (2007), (eds) Tectonics of Strike-Slip Restraining and Releasing Bends, Geol. Soc. Of London, Special Publications, 290, 1-12.

Cunningham, W.D., Structural and topographic characteristics of restraining bend mountain ranges of the Altai, Gobi Altai and easternmost Tien Shan, from Tectonics of Strike-Slip Restraining and Releasing Bends, Cunningham, W.D. and P. Mann (eds), Geol. Soc. of London, 290, 219-238.

Curren, I.S. and P. Bird (2014), Formation and suppression of strike-slip fault systems, *Pure and Applied Geophysics*, 1-20.

DeGroot, D.J., Lunne, T., 2007. Measurement of Remoulded Shear Strength. Norwegian Geotechnical Institute. Report 20061023-1.

Del Castello, M., G.A. Pini, K.R. McClay (2004), Effect of unbalanced topography and overloading on Coulomb wedge kinematics: Insights from sandbox modeling, *Journal of Geophysical Research*, 109.

Demets, C., R.G. Gordon, D.F. Argus (2010), Geologically current plate motions, *Geophs. J. Int.*, 181, 1-80.

Eisenstadt, G., and D. Sims. "Evaluating Sand and Clay Models: Do Rheological Differences Matter?" *Journal of Structural Geology* (2005): 1399-412.

Fialko, Y., L. Rivera, H. Kanamori (2005), Estimate of differential stress in the upper crust from variations in topography and strike along the San Andreas fault, *Geophys. J. Int*, 160, 527-532.

Gomez, F.,T. Nemer, C. Tabel, M Khawlie, M. Meghroui, M. Barazangi (2007), Strain Partitioning of Active Transpression Within the Lebanese Restraining Bend of the Dead Sea Fault (Lebanon and SW Syria), from Tectonics of Strike-Slip Restraining and Releasing Bends, Cunningham, W.D. and P. Mann (eds), Geol. Soc. of London, 290, 285-303.

Haeussler, P.J. (2008), An overview of the neotectonics of interior Alaska: Far-field deformation from the Yakutat Microplate Collision, *Active Tectonics an seismic potential of Alaska*, AGU Monograph Series 109, 83-108.

Henza, A., M. O. Withjack, and R. W. Schlische (2010), Normal-fault developmsent during two phases of non-coaxial extension: An experimental study, J. Struct. Geol., 32, 1656–1667

Malavielle, J. (2010), Impact of erosion, sedimentation, and structural heritage on the structure and kinematics of orogenic wedges: Analog models and case studies, *GSA Today*, 20, 4-10.

Matti, J. C., and D. M. Morton (1993), Paleogeographic evolution of the San Andreas fault in Southern California: A reconstruction based on a new cross-fault correlation, Mem. Geol. Soc. Am., 178, 107– 159.

Matti, J. C., D. M. Morton, and B. F. Cox (1992), The San Andreas fault system in the vicinity of the central Transverse Ranges province, Southern California, U.S. Geol. Surv. Open File Rep., 92–0354.

McClay, K., and M. Bonora (2001), Analog models of restraining stepovers in strike-slip fault systems, *AAPG Bulletin*, 85 (2), 233-260.

McGill, S.D., L.A. Owen, R.J. Weldon II, K.J. Kendrick (2013), Latest Pleistocene and Holocene slip rate for the San Bernardino strand of the San Andreas fault, Plunge Creek, Southern California: Implications for strain partitioning within the southern San Andreas fault system for the last ~35 k.y., GSA Bulletin, 125 (1), 48-72.

Mitra, S. and D. Paul (2011), Structural geometry and evolution of releasing and restraining bends: Insights from laser-scanned experimental models, AAPG Bulletin, 95 (7), 1147-1180.

Oertel, G. (1965), The mechanism of faulting in clay experiments, Tectonophysics, 2, 343-393.

Paul, D., and S. Mitra (2013), Experimental models of transfer zones in rift systems, *AAPG Bulletin*, 97, 759-780.

Reilinger, R., et al. (2006), GPS constraints on continental deformation in the Africa-Arabia-Eurasia continental collision zone and implications for the dynamics of plate interactions, J. Geophys. Res., 111,

Schlische, Roy W., Martha O. Withjack, and Gloria Eisenstadt. "An Experimental Study of the Secondary Deformation Produced by Oblique-slip Normal Faulting." *American Association of Petroleum Geologists Bulletin* 86.5 (2002): 885-906.

Shelef, E. and M. Oskin (2010) Deformation processes adjacent to active faults: Examples from eastern California, Journal of Geophysical Research, 115.

Scholz, C. H. (2002). *The mechanics of earthquakes and faulting*. Cambridge university press.

Slominski, C., Niedostatkiewicz, M., & Tejchman, J. (2007). Application of particle image Velocimetry (PIV) for deformation measurement during granular silo flow. *Powder Technology*, *173*(1), 1-18.

Swanson, M.T. (2005), Geometry and kinematics of adhesive wear in brittle strike-slip fault zones, *Journal of Structural Geology*, 27, 871-887.

Titus, S.J., B. Housen, B. Tikoff (2007), A kinematic model for the Rinconada fault system in central California based on structural analysis of *en echelon* folds and paleomagnetism, *Journal of Structural Geology*, 29, 961-982.

Wakabayashi, J., J.V. Hengesh, T.L. Sawyer (2004), Four-dimensional transform fault processes: progressive evolution of step overs and bends, Tectonophysics, 392, 279-301.

Wakabayashi, J. (2007), Stepovers that migrate with respect to affected deposits: field characteristics and speculation on some details of their evolution, from *Tectonics of Strike-Slip Restraining and Releasing Bends,* Cunningham, W.D. and P. Mann (eds), Geol. Soc. Of London, 290, 169-188.

Withjack, M.O., Q.T. Islam, and P.R. La Pointe. "Normal Faults and Their Hanging-Wall Deformation: An Experiment Study." *American Association of Petroleum Geologists Bulletin* 79.1 (1995): 1-18.

Yule, D. and K. Sieh (2003), Complexities of the San Andreas near San Gorgonio Pass: Implications for large earthquakes, Journal *of Geophysical Research*, 108.

Veenstra, E., D.H. Christensen, G.A. Abers, A. Ferris (2006), Crustal thickness variation in south-central Alaska, *Geology*, 34, 781-784.

CHAPTER 2

STRAIN LOCALIZATION AND EFFICIENCY IN WET KAOLIN EXPERIMENTS OF INITIATING STRIKE-SLIP FAULTS

2.1 Abstract

Strike-slip fault initiation includes the coalescence and linkage of fault segments dependent on changing material properties and boundary conditions. Wet kaolin analog modeling is an apt tool to add directly observe strike-slip initiation. We document how strain localizes onto a strike-slip fault in wet kaolin physical models by varying the thickness of the clay, the nature of the basal boundary and the initial fault condition (incorporating a pre-cut fault or not). In experiments with a pre-cut fault, the shear zone localizes quickly to a narrow fault surface. When no fault is cut prior to displacement, strain localizes onto short, echelon faults oriented for extension in a dextral system. These fractures propagate, slip, in some cases, overlap, and abandon to eventually develop a throughgoing strike-slip fault. This final fault is irregular in experiments without a pre-cut fault, primarily in thick experiments and/or without a localized basal plate condition. Although some shear fractures overlap during the fault development, we observe active stepovers in the experimental faults that may or may not persist throughout the experiment. We do observe a persistently wide shear zone and preserved deformation zone surrounding the fault. Narrowing shear zones of the incipient fault increases strike-slip efficiency with three stages in uncut experiments. Stage 1 is a sustained, wide shear zone with diffuse shear strain above the localized or distributed shear at the base of experiment about the incipient fault. In this stage, strike-slip efficiency is zero. Stage 2 involves rapid narrowing of the shear zone, as a decrease in

distributed deformation corresponds with rapid increase in strike-slip efficiency. Stage 3 involves a prolonged period of a fault coalescence as the initial echelon faults link together to form a single throughgoing fault surface. In this stage 3, strike-slip efficiency continues to increase, but not as rapidly as in stage 2. The irregularity in fault trace (stepover distance between faults) is maximized during stage 3, and off-fault deformation is concentrated between overlapping faults. Finally, all fault zones narrow, as a single slip plane observed on the clay surface. Pre-cut faults are up to 98% strike-slip efficient, while uncut faults are about 90% efficient at best.

2.2 Introduction

Idealized strike-slip faults observed in wet kaolin experiments efficiently accommodate applied deformation (Hatem et al., in prep). Yet, crustal strike-slip faults are very complex and are not as idealized as previous clay models. Crustal strike-slip systems accommodate a significant portion of applied loading as off-fault deformation (Herbert et al., 2014; Shelef and Oskin et al., 2010; Titus et al., 2007). Additionally, strike-slip rates within fault systems can evolve over time, with particular faults systems within a plate boundary clustering in either periods of earthquake activity or "lulls" (Dolan et al., 2007; Sharp 1981; Dawson et al., 2003). Strike-slip faults can accommodate off-fault deformation and variable strike-slip rates as plate motion vectors change over time (i.e. Gomez et al., 2007; Herbert and Cooke 2012). Strike-slip fault systems may also have discontinuous faults that over- or underlap, forming restraining or releasing stepovers. Such structures are mechanically inefficient initially, but evolve over time to accommodate more than 80% of applied deformation as strike-slip (Cooke et al., 2013;

Hatem et al., in prep). Despite the mechanically inefficiency of stepovers caused by accumulating convergence or extension within a bend in the fault, restraining and releasing bends persist along crustal strike-slip faults.

As strike-slip faults initiate and develop, echelon fractures and faults form first, eventually linking up to form a continuous yet irregular strike-slip fault in crustal systems (e.g. Crider and Peacock, 2003; Segall and Pollard, 1983) and in analog models (e.g. Wilcox et al., 1973; An and Sammis 1996). Once this fault is established, strike-slip occurs in a very narrow zone in the center of the principal displacement zone along a fault plane, with a wide, permanent deformation zone surrounding the fault core (e.g. Caine et al., 1996). The width of the deformation zone may influence how efficient incipient strike-slip faults are at partitioning strain as strike-slip instead of off-fault deformation. For example, the Calico fault did not rupture in either the Landers or the Hector Mine earthquakes but appeared to accommodate some coseismic strain (observed with INSAR) (Cochran et al., 2009). Upon seismic investigation, workers revealed the Calico fault had a much wider damage zone than the surrounding faults that did rupture in the Landers and Hector Mine events (Cochran et al., 2009).

A persistently wide damage zone may influence the amount of off-fault deformation accommodated as a strike-slip fault initiates. Off-fault deformation may persist for longer temporally and over a greater spatial distribution within the initiating strike-slip fault system when boundary conditions are varied. We explore the effect of clay thickness, nature of basal slip (localized versus distributed), and preexisting faults on the localization of strain into a continuous fault, and how this localization effects the efficiency of the fault. We test the differences between systems with a pre-cut versus an

uncut fault to understand the effect of propagating shear fractures on strike-slip fault initiation. Additionally, we examine the differences between thin and thick claypacks to understand any depth dependency during strike-slip initiation. Finally, we manipulate the basal plates of the claybox to represent either localized or distributed basal shear to quantify the effect of basal conditions on propagation of initiating strike-slip faults. We correlate the evolution of the shear zone and structural evolution of the damage zone to strike-slip efficiency using the changing width of the damage zone, shear strain maps of the clay surface, vertical axis rotation, fault overlap and fault roughness. We expect the shallow, localized shear zone with a pre-cut fault to localize strain with the least amount of plate displacement, and to also have the greatest strike-slip efficiency. In turn, we expect the deep, distributed shear zone without pre-cutting the fault to require the most plate displacement to localize strain and be the least strike-slip efficient. We choose these parameters to attempt to understand mechanical differences between fault systems. For instance, in New Zealand, Porter's Pass-to-Amberly Fault Zone (PPAFZ) is structurally immature compared to the Hope fault to the north of the PPAFZ (Cowan et al., 1996 Figure 1E). The differences in structural maturity appears to account for a factor of 5 difference in recurrence interval of large earthquakes between the PPAFZ and Hope fault, with events occurring on the PPAFZ less frequently than the Hope fault (Cowan et al., 1996).

2.3 Methods

We utilize scaled, analog models of wet kaolin for this work to understand processes typically spanning millions of years over large spatial regions in just a few hours within a

laboratory. Scaled analog models provide a quantitative and qualitative method to capture complete events and processes we could otherwise only observe portions within the greater process in the field.

2.3.1 Wet Kaolin

This analog modeling study utilizes wet kaolin as the modeling material, for reasons detailed in Eisenstadt and Sims (2005), Schlishe et al. (2002), Henza et al. (2010), Cooke and van der Elst (2012), Cooke et al. (2013) and Hatem et al. (in prep). In short, wet kaolin can grow discrete, localized faults, which is necessary in a study of fault evolution. Additionally, wet kaolin is a Burger's material with elastic and viscous properties. Wet kaolin is an appropriate material because the coefficient of friction of wet kaolin is equitable to that of the Earth's crust, faults in wet kaolin are capable of reactivating, and wet kaolin can be easily scaled in strength and length to the Earth's crust by manipulating the water content (and associated shear strength) of the clay using water. Water content of the wet kaolin is 65-70%, with only ~2% water loss during the experiments detailed in this study. The density of the wet kaolin is about 1.6g/cm^3, and considering a density of continental crust as 2.65 g/cm^3 with a shear strength of 10-20 MPa, we add enough water to the wet kaolin to yield at a shear strength of 90-115 Pa. As such, the length scaling is 1cm in the claybox is equal to 0.75-1.4km of continental crust. Roughly, the claybox is five orders of magnitude smaller and weaker than continental crust.

2.3.2 Claybox

We use the same experimental rig detailed in Cooke et al. (2013) and Hatem et al., (in prep). This claybox is a motor controlled, table-top laboratory rig designed to simulate crustal faulting. One side of the box is attached to the table, and the other is attached a computer controlled stepper motor. The motor moves at 0.5 mm/minute in dextral, horizontal (x) slip for all experiments discussed here. Prior to displacement, we sprinkle red and black sand on top of the light beige wet kaolin to provide contrast in images for particle tracking (see PIV section). We also demarcate reference lines perpendicular to the direction of motion. The reference lines provide a simple, qualitative way to examine the off-fault deformation, as well as slip along fractures, during and after the experiment.

In experiments with a pre-cut fault, we cut the fault using a template that exactly mimics the basal detachment (boundary between the two plates parallel to motor movement) with an electrified probe through the entire depth of the claypack (Figure 1A). We use an electrified probe to reduce puckering of the clay. In pre-cut experiments, we provide an ideal plane for strike-slip; results from a model such conditions provide a control experiment. Uncut experiments, however, are more realistic when comparing experimental results to crustal faults. In experiments where we attempt to simulate localized basal shear, the plates are left as is with the stationary plate abutting, but not over or underlapping, the moving plate (Figure 1B). In contrast, we run experiments when the plates are separated by a 1.5cm wide Theraband© elastic resistance band, simulating distributed basal shear (Figure 1C). The Theraband© is glued to the bottom of each plate. In experiments simulating a deep shear zone, the claypack is 5cm thick; in

experiments simulating a shallow shear zone, the claypack is 2.5cm thick. Thicker experiments may have a wider damage zone than thinner experiments.

In total, we investigate six unique experiments, which are schematically illustrated in Figure 1D. We code the different experiments at times throughout the paper for brevity. The first letter refers to the initial condition of the fault, either pre-cut ("P") or uncut ("U"). The second letter refers to the basal shear condition as either the plate ("P") or elastic ("E"). The third letter refers to the depth of shear zone, either thin ("N" as thiN) or thick ("K" as thicK). We use the graphics shown in Figure 1D throughout this work in legends of figures, but refer to the experiments as their three letter code in the text.

2.3.3 Particle Image Velocimetry

We employ Particle Image Velocimetry (PIV) to collect data from the claybox experiments (i.e. Adam et al., 2004). We collect images from above the claybox rig throughout the experiment. The suspended camera shoots remotely at one minute intervals (0.5mm of applied displacement). Image resolution is typically 90 pixel/cm. We process the images through PIV after distorting the images for lens effects. PIV recognizes and tracks pixels moving through a 25 by 25 pixel window within a region of interest we select from the larger experimental field of view. When selecting a region of interest, we avoid the boundaries of the claybox to minimize boundary effects in the physical model while capturing the most deformation possible. From PIV, we can analyze the velocity in horizontal and vertical plane to determine the shear strain rate fields. For more on the application of PIV in analog studies, please refer to Hatem et al., (in prep) and references therein.

2.4 Results

We analyze the process of strike-slip initiation by quantifying the evolving geometry of faults over time as distribution of shear strain within the system, the narrowing shear zone over time and the ability of the system to minimize off-fault deformation.

2.4.1 How does strain localize onto initiating strike-slip faults?

The process by which strain localizes onto a continuous fault surface as a strike-slip fault initiates is complex, yet stepwise. We can observe such processes by examining the spatial distribution of shear strain, as well as the narrowing shear zone about the principal displacement zone where the strike-slip fault will later initiate.

2.4.1.1 Spatial evolution of shear strain

Mapping shear strain within a fault zone highlights areas of the claybox where distributed strain is accommodated. A shear zone is an area where shear deformation is diffuse. Such a zone is captured well in incremental shear strain maps (Figures 2 and 3). In crustal systems, we can observe the cumulative shear strain within a system but determining incremental shear strain is difficult, if not impossible. We show incremental shear strain maps here to determine how shear strain evolves over time. We describe the endmember experiments (PPN and UEK); all experiments may be viewed in animations in the Supplemental Information.

Experiment PPN (pre-cut, plate, thin) initially has a fairly narrow shear zone about the pre-cut fault, captured at 2mm of plate displacement (Figure 2A). Despite the

diffuse shear strain around the fault, the fault has already accumulated shear strain after only 2mm of plate displacement. Within this narrow shear zone, most of the diffuse shear is concentrated above the moving plate. By 9mm of plate displacement, shear strain has further localized to a very small shear zone about the slipping fault (Figure 2B). At 14mm of plate displacement, the fault is slipping only along the pre-cut fault (Figure 2C).

In contrast, experiment UEK (uncut, elastic, thick) strain localization process persists over more applied plate displacement, and the stages of strain localization are more obvious. At 13mm, practically the plate displacement at which experiment PPN had localized all strain as strike-slip along a single fault, experiment UEK still has a wide, distributed shear zone (Figure 3A). By 22mm of plate displacement, this shear zone narrows as strain localizes onto faults at the left and right edges of the region of interest (Figure 3B). The width of the shear zone is not uniform along the length of the fault, and is widest in the middle of the region of interest (Figure 3B). At 36mm of plate displacement, strain has localized onto multiple faults (Figure 3C). In this map, two, long echelon faults have overlapped over almost their entire length. These initial faults still have diffuse deformation surrounding the individual faults, despite the larger shear zone localizing most strain onto the faults; diffuse deformation still persists within the system after most strain has localized. Off-fault deformation is negligible by 48mm of plate displacement (Figure 3D). At this point, a portion of the overlapping fractures is abandoned in favor of connecting the shear fractures to form a throughgoing, continuous fault, which is observed at 60mm of plate displacement (Figure 3E). Although a throughgoing, continuous fault has developed, the fault is not straight and is instead irregular along its length (Figure 3F).

We can define three distinct stages of strike-slip fault initiation as the shear strain distribution evolves over time within the system. Stage 1 involves diffuse deformation about the principal displacement zone (Figures 2A, 3A). Stage 2 consists of strain localizing onto the precut fault, if present, or echelon faults within a fairly narrow shear zone (Figures 2B and 3B, C). Stage 3 is the period of the experiment when slip is localized incrementally onto a throughgoing fault surface, which, in experiments with an uncut fault, is irregular and contains overlapping fault segments. The system accommodates strike-slip along a continuous fault after stage 3. All experiments tested exhibit these stages, although stage 3 is quite brief in the pre-cut experiments. These stages of fault initiation apply to the evolutions of the shear zone about the principal displacement zone, strike-slip accommodation and fault roughness. Other workers have developed a similar three stage process of strike-slip initiation in systems that contain preexisting structures (Crider and Peacock 2003). In this schema, stage 1 is when shear is accommodated along the preexisting structures, stage 2 is when these structures link, and stage 3 is the development of a throughgoing fault (Crider and Peacock 2003). When considering systems without preexisting structures, as the models with uncut faults, stage 1 as categorized by Crider and Peacock (2003) may not be appropriate because strain needs to localize onto fractures before advancing in the process of fault initiation.

2.4.1.2 Shear zone evolution

In shear strain maps, we can qualitatively observe a narrowing shear zone. However, we can quantify shear zone width as the width within the claybox where displacement is greater than 0mm/min and less than plate rate (0.5mm/min) (Figure 4). In Figure 4A, we plot the mean shear zone width as a function of plate displacement. We

also plot mean shear zone width as a function of cumulative plate strike-slip within the fault system (Figure 4B). In both cases, we plot mean shear zone width, as we already observed the shear zone width is variable along fault length (Figure 3B, 4C). Observing evolving shear zone width versus experiment time (applied plate displacement) shows how strain localizes throughout the entire experiment, whereas analyzing shear zone width against cumulative strike-slip shows strain localization behavior only after the onset of strike-slip within the fault system. Shear zone width is a good indication of strain localization, as a narrower shear zone includes more localized slip along faults (Figures 2 and 3).

As noted in discussion of Figure 3, the shear zone evolves as strain localizes in three distinct stages. These stages are evidenced as significant changes in slope when mean shear zone width is plotted against both plate displacement and cumulative strike-slip. In Figure 4A, stage 1 is represented as an initial plateau (slope =0) in shear zone width, showing deformation is diffuse and is unchanging in width about the principal displacement zone; stage 2 is the fairly rapid to rapid negative slope, following stage 1, as the shear zone narrows; stage 3 is represented by a negative slope just greater than 0 when strain slowly localizes from a fairly narrow zone onto a very narrow fault surface. In Figure 4B, stage 1 is not represented, as stage 1 only occurs after the onset of slip, and Figure 4B only begins plotting data when the system begins to accommodate strike-slip. However, stages 2 and 3 are represented as an initial rapid decrease in shear zone width, followed by a slower narrowing in shear zone width. In both methods of plotting, stage 3 is followed by slip along a consistently narrow fault surface (change in shear zone width ~ 0).

The pre-cut experiments have narrower initial shear zones and localize strain with less applied plate displacement and cumulative strike-slip when compared to experiments with an uncut fault (Figure 4). The pre-cut faults (experiments PPN and PPK) require a small amount of plate displacement to narrow the shear zone. In Figure 4A, this short initial period of localization, stage 1, is represented by a plateau of shear zone with (~6-7cm width) and persists for the first 7-8 mm of applied plate displacement. Stage 1 doesn't end in systems uncut fault until as late as 20mm of plate displacement (Figure 4A). Pre-cut faults have very short stages 1 and 2, in which the shear zone rapidly narrows as strain localizes onto a throughgoing fault. This process is achieved in only ~4 mm of plate of displacement; the shear zone is completely localized by 13mm of plate displacement. In contrast, uncut experiments remain in stage 2 for as few as 5 or as many as 10mm of plate displacement, with stage 3 persisting for as much as 15mm of plate displacement (Figure 4A). Additionally, the standard deviation in experiments with a pre-cut fault is quite small compared to that of the uncut experiments, as shown with the narrow band bounding each curve in Figure 4A. The rapid fault development of pre-cut faults is also evidenced by the near immediate decrease in shear zone width plotted against cumulative strike-slip (Figure 4B). Experiments with an uncut fault do not localize strain within a narrow fault zone until ~20mm of cumulative strike-slip (Figure 4B). The differences in length of stage 3 between precut and uncut faults is most evidenced in Figure 4B as pre-cut faults rapidly change slopes at about 3-5 mm of cumulative strike-slip. Uncut faults change slopes from a rapidly thinning shear zone until 3-5mm of cumulative strike-slip, but require 10-15mm (or more) of cumulative strike-slip within the system to reduce the slope to near 0 (Figure 4B).

Clay thickness controls the initial width of the shear zone, as well as the length of the experiment (applied plate displacement) systems remain in a given stage; thicker experiments have initially wider shear zones and a slower strain localization than thinner experiments. For instance, comparing experiments UEN and UEK shows the thinner experiment has narrower initial shear zone in stage 1 at 7-8cm wide compared to 10-12 cm wide in the thicker experiment (Figure 4A). Despite the shear zones in both UEN and UEK ending stage 2 at about 3mm of cumulative strike-slip, UEN shear zone is nearly a centimeter wider at the start of stage 3 (Figure 4B). Additionally, UEN begins stage 3 at about 18mm of applied plate displacement, whereas UEK begins stage 3 around 25 mm of plate displacement, showing thicker systems require more plate displacement to accumulate the same amount of cumulative strike-slip (Figure 4A,B). All thick experiments require more plate displacement to initially narrow the shear zone, even the experiments with a pre-cut fault (Figure 4A). Thickness of the clay has a strong effect on the timing of strain localization process to initiate a strike-slip fault.

The basal plate conditions controls has only minor effects on narrowing of the shear zone within the experiments tested; these effects are most evident in the thinner experiments (Figures 4A, B). The system with an uncut fault with an elastic basal insert in a thin claypack has an initially wider shear zone than the experiment with an uncut fault without an elastic basal insert in a thin claypack, with UEN having an initial shear zone 7.5 cm wide compared to 6 cm in UDN Figure 4A). Additionally, experiment UEN remains in stage 1 for longer, as the onset of slip doesn't begin until about 17mm of plate displacement here; in UDN, begins to localize strain at about 12mm of plate displacement (Figure 4A). Model UEN also remains in stage 2 longer than UDN, requiring an elapsed

17mm of plate displacement to completely narrow the shear zone, whereas UDN begins to slip along a narrow fault surface after localizing strain for only about 5mm of plate displacement (Figure 4A). Most noticeable is the final fault zone is wider in experiments with an elastic basal insert (UEN, UEK) compared to those without (UDN, UDK) (Figure 4B). Within standard deviation, though, the fault zones are all comparably thin (Figure 4A).

2.4.2 How do initiating strike-slip faults accommodate tectonic loading?

To measure how initiating strike-slip faults accommodate applied plate displacement, we quantify the strike-slip efficiency of the evolving fault system. Strike-slip efficiency of faults within a system, we take the percentage of the amount of plate displacement accommodated as strike-slip (displacement in the x direction) (Cooke et al., 2013; Hatem et al., in prep). If strike-slip efficiency is equal to 100%, all applied plate displacement is accommodated as strike slip. If strike-slip efficiency is anything less than 100%, some applied displacement must be manifested as off-fault deformation, such as vertical axis rotation. Strike-slip efficiency allows us to understand, on a gross level, strain partitioning within the initiating strike-slip fault systems studied. We analyze strike-slip efficiency as a function of plate displacement, as well as plotting the plate displacements at which each experiment achieves a specific milestones of strike-slip efficiency (onset of slip as non-zero efficiency, 45% and 90%). We chose such milestones because all experiments reach at least 90% strike-slip efficiency in the experiment length tested. Plotting the evolution of strike-slip efficiency over time shows the system wide mechanical evolution; plotting the milestones of efficiency distills

critical information from the overall mechanical evolution to show strike-slip efficiency increases incrementally in each experiment.

The experiments with a precut fault have a strike-slip efficiency evolution distinct from uncut faults, in the sense that faults in these models slip sooner and accommodate more strike-slip per mm of plate displacement (Figure 5A). Experiment PPN is the only experiment tested with a fault that exhibits an initial increase with an immediate decrease in strike-slip efficiency from 3mm-6m of plate displacement (Figure 5). Hatem et al. (in prep) observe a similar behavior in wet kaolin analog models of pre-cut restraining bends in thin claypacks. Such behavior was previously attributed to pre-cutting the fault and fluid flow along the pre-cut plane. However, we do not observe this behavior in PPK, showing this initial increase and decrease may not be solely dependent on pre-cutting the fault, and instead have some depth dependence (Figure 5). Both experiments with a pre-cut fault end stage 1 of a diffuse shear zone at the onset of slip around 7-8mm, if ignoring the immediate increase in strike-slip efficiency in experiment PPN (Figure 5A). In contrast, uncut experiments do not begin to slip until 15-20mm of plate displacement (with the exception of experiment UPN) (Figure 5A). By about 12mm of plate displacement, both PPN and PPK are highly efficient, and end stage 2 quite rapidly. The initial increase in strike-slip efficiency can be attributed to the narrowing shear zone about the principal displacement zone. In experiments with an uncut fault, stage 2 occurs over a slightly longer period of plate displacement, lasting for as short as 7mm or as long as 12mm of plate displacement. The largest contrast between experiments with pre-cut and uncut faults is, again, the duration of stage 3 (Figure 5A). For instance, in model PPK, stage 3 persists from 10-14mm of plate displacement; in model UEK, stage 3

persists from 26-55mm of plate displacement (Figure 5A). Within the limits of the applied experimental plate displacement, models with pre-cut faults become up to 98% strike-slip efficient, and models with uncut faults evolve to become up to 92% strike-slip efficient (Figure 5A). Perhaps, if experiments were continued for more applied plate displacement, uncut experiments may further evolve to accommodate as much strike-slip per mm of applied displacement as pre-cut faults. From Figure 5B, we see that the evolution of strike-slip efficiency in models with a pre-cut fault are temporally symmetric. That is to say, the system requires nearly similar amounts of applied plate displacement to increase the efficiency of the system from 0-45%, and then again from 45-90%. Pre-cut experiments have a very asymmetric evolution of strike-slip efficiency. The systems quickly increase the strike-slip efficiency of growing faults from 0-45%, but require at least double, and sometimes more than five times, that amount of plate displacement to increase strike-slip efficiency from 45-90%. The initial condition of the fault within the model controls the onset of slip, as well as the amount of plate displacement required to make modeled fault systems highly strike-slip efficient.

Doubling the thickness of the claypack increases the amount of plate displacement required for the onset of slip within the system, and also increases the amount of plate displacement required to transition from stage 3 to a throughgoing fault. For instance, model UPN begins stage 2 at 8mm of plate displacement, compared to about 17mm of plate displacement in UPK (Figure 5A). Likewise, model UEN begins stage 2 at around 14mm, whereas UEK starts slipping at 20mm of plate displacement (Figure 5A). Stage 3 is quite brief in experiment UPN, lasting only from about 16-20mm

of plate displacement, compared to 18mm of elapsed plate displacement spanning stage 3 in model UPK (Figure A).

The basal plate condition appears to control where faults are initiate within the claypack. The onset of slip along faults in experiment UPK is nearly double that of experiment UPN (Figure 5). As the claypack in model UPK is two times as thick as UPN, we can assume that faults initiate from the basal plate discontinuity (localized shear) and propagate upwards from below. However, this hypothesis does not hold true in experiments with an elastic insert on the basal plate (distributed shear). The onset of slip in experiment UEK is not double that of UEN, and is instead roughly equal (separated by only about 4mm of plate displacement) (Figure 5). This observation negates the upward propagation hypothesis proposed for localized basal shear, and instead implies that faults grow within the claypack when basal shear is distributed (Figure 5
B).

Experiment UEK has an interesting behavior from 25-38mm of plate displacement, where the strike-slip efficiency slightly plateaus, decreases, then increases again. The UEK system actually accommodates a noticeable increase in off-fault deformation as the system is typically gaining fault slip and losing off-fault deformation. We only observe such partitioning behavior in this experiment, and only during stage 3.

2.4.3 Is the narrowing shear zone related to increasing strike-slip efficiency?

The stages observed in Figure 4 are the same stages observed in Figure 5, meaning shear zone width and strike-slip efficiency are dependent on each other. Strike-slip efficiency increases as shear zone with decreases (Figure 6A). The two variables have a strong anti-correlation, with $R^2 = 0.93$ in a quadratic fit of all experiment data (all

experiments combined into one data set) (Figure 6A). The quadratic fit captures the entire data set; completing only a linear fit shows a poor fit if including the tail of data prior to the onset of slip (strike-slip efficiency = 0%).

The anti-correlation shows the how the stages of fault initiation relate between shear zone width and strike-slip efficiency, for example, in experiment UEN (Figure 6B). The changes in slope of shear zone width and strike-slip efficiency representing changes in initiation stages are very similar between shear zone width and strike-slip efficiency. In stage 1, shear zone width decreases with no change in strike-slip efficiency (Figure 6B). In stage 2, data points are widely distributed over a short period of plate displacement (few data points), when shear zone narrows rapidly as strike-slip efficiency rapidly increases (Figure 6B). In stage 3, minimal changes in shear zone width correspond to increases in strike-slip efficiency; many data points are included in this stage, showing stage 3 persists for longer duration than stage 2 (Figure 6B). Finally, when slip is localized onto a continuous fault, very little to no change is observed in either strike-slip efficiency or shear zone width (Figure 6B).

We observe small differences in stage 2 and 3 between pre-cut and uncut faults (Figure 6C). Pre-cut faults are more efficient in the same shear zone width when compared to uncut faults in stage 2 (Figure 6C). Likewise, in stage 3, pre-cut faults have the same strike-slip efficiency in narrower shear zones (Figure 6C). Such observations indicate the importance of preexisting structures on slip localization in initiating strike-slip faults.

2.5 How do growing faults interact and effect the strike-slip efficiency of the system?

As faults grow, coalesce, overlap, abandon and link, particularly in stage 3 of strike-slip initiation, fault interactions influence the accommodation of off-fault deformation within the system. Persistent off-fault deformation contributes to a longer lived stage 3 in fault initiation.

2.5.1 Fault Roughness

Fault roughness meausres the changing irregularity of fault surface trace over time, showing periods of the experiment to have straight or wavy fault geometry (review Figures 2 and 3 for an example of how the fault surface changes over time). We define fault roughness after Candella et al. (2009) and Schmittbuhl et al. (1993), by measuring the maximum and minimum height of active fault within a band of finite length passing across the entire region of interest. We select a band width of three 25 pixel windows wide (75 pixels total), which is 0.75-1cm wide depending on the cm/pixel scale in a given experiment. We then calculate the root mean square (RMS) of the range in height in each window, and average the RMS of all band samples across the length of the region of interest for each time step (0.5mm of applied deformation). This measure of fault roughness indicates the changing irregularity of fault surface trace over time (Figure 7). We observe noticeably rough faults only in experiments UPK, UEN and UEK, and will only discuss those experiments in the coming section for that reason.

In models UPK, UEN and UEK, we observe the roughest fault surface trace during stage 3 of fault initiation (Figure 7). For an example of an image of rough or overlapping faults, compare the UEK roughness curve to the shear strain maps of Figure 3. The maximum fault roughness occurs 5-10mm of plate displacement after the stage 3

begins, when strike-slip efficiency increases at a much slower rate. The roughest fault is UEK, and this peak in roughness corresponds well with the local minimum in strike-slip efficiency at 33mm of plate displacement. Here, in experiment UEK, we see that increasing roughness actually increases the amount of off-fault deformation within the system. At their maximums, UEK is rougher than UEN by about 1cm, and UEN is rougher than UPK by about 1 cm. The basal plate condition has a large effect on roughness; UEK is about 2cm rougher than UPK at their maximum roughness. Slipping above the elastic basal insert appears to make the fault surface trace rougher than experiments without the insert (we observe little to no roughness in experiment UPN). Experiments UPK and UEK decrease roughness and become straighter after the end of stage 3, when slip is accommodated along a continuous fault surface. However, experiment UEN increases roughness when strike-slip efficiency is steady at about 90%. Overlapping faults are persistent in this model, despite having a high ratio of fault slip to off-fault deformation.

2.5.2 Vertical Axis Rotation

In these dextral systems, we expect to observe clockwise rotation along the faults. However, as faults overlap, they spatially contain areas of counterclockwise rotation (Figure 8). As roughness decreases and overlapping faults link, counterclockwise rotation can still persist, showing that even small irregularities along the fault trace can concentrate regions of counterclockwise rotation. In Figure 8, cumulative vertical axis rotation summed only between 30 and 45 mm plate displacement has a different spatial distribution within the model UEK than the cumulative vertical axis rotation summed only between 45 and 60 mm plate displacement. When the fault is roughest, from 35-

50mm of plate displacement, counterclockwise rotation is diffuse between overlapping faults (Figure 8A). Faults are rotating in concentrated clockwise rotation; fault locations can also be reviewed in Figure 3. However, when the fault becomes more regular along its strike, counterclockwise rotation is concentrated in areas where the stepovers persist (Figure 3E, 8B). Decreasing fault roughness decreases the amount of counterclockwise rotation along an initiating dextral strike-slip fault.

2.6 Discussion

Contextualized observations in the claybox can be extrapolated to theories of crustal fault evolution. Here, we discuss some interpretations of claybox data with respect to the Earth's crust.

2.6.1 How efficient is efficient enough?

Despite all experiments evolving to minimize off-fault deformation, the strike-slip efficiency never reaches 100%. Yet, the faults are very efficient accommodating 90%+ of applied deformation as strike-slip. As noted in Figure 5, initially increasing strike-slip efficiency from 0-45% requires much less plate displacement than increasing efficiency from 45% to 90%. The evolution of strike-slip efficiency within the initiating fault system is dependent on many factors, primarily boundary conditions. Boundary conditions influence changes in strike-slip efficiency, as well as fault structure, shear zone width (i.e. strain localization), vertical axis rotation, fault segment overlap and fault surface irregularity. All experiments have an asymmetric fault development, meaning the systems achieve high strike-slip efficiency with less plate displacement than it takes to maximize strike-slip efficiency. Processes that could control this are fault plane

smoothing (reduction of roughness along fault plane), fluids flowing into and along the fault plane, or minute geometric changes to accommodate as much strike-slip as possible (i.e. gradual decrease in fault roughness throughout the second half of stage 3). Achieving the last 10% of the strike-slip efficiency, for instance, in uncut experiments, is a process we do not observe within the experimental plate displacement. Perhaps, over a much longer experiment, we could observe all modeled fault systems achieve 100% strike-slip efficiency.

Despite this high efficiency, we observe stepovers in fairly efficient systems (Figure 7). However, the strike-slip efficiency appears to get steadier and changes less with each unit of applied plate displacement as the fault roughness decreases (Figure 7). Even still, model UEN has actively widening stepovers when strike-slip efficiency is steady at about 90-92% (Figure 7). As such, we can say that stepovers, and perhaps including incipient restraining or releasing bends, are inefficiencies which are typically abandoned to achieve high strike-slip efficiency along the fault. Prior wet kaolin analog studies demonstrate that restraining bends evolve to maximize strike-slip efficiency (Cooke et al., 2013; Hatem et al., in prep). Perhaps, stepovers along strike-slip systems persist as the strike-slip system is moderately to highly strike-slip efficient with an evolving stepover along that fault. The individual stepover, as shown by Cooke et al. (2013) and Hatem et al. (in prep), mechanically evolves as its own system within a larger strike-slip fault. As the faults in this study smooth as off-fault deformation is minimized, large gains in strike-slip accommodation are made within each stepover as they evolve. As such, stepovers in crustal systems may be persistent over geologic time. However, the entire system may be efficient enough despite these local mechanical inefficiencies where

off-fault deformation concentrates. A highly strike-slip fault will likely contain pockets of off-fault deformation, perhaps expressed as counterclockwise rotation (Figure 10.5). On a larger scale, though, the entire fault accommodates nearly all applied deformation as strike-slip.

2.6.2 How can analog observations contextualize crustal strike-slip faults?

Because our models and wet kaolin strength is carefully scaled, the results of our analog models can be extrapolated to initiating strike-slip fault systems in the Earth's crust. The scaled timescales represented in the analog models depends on the specific crustal system plate rate (Figure 9). In a slow moving system (i.e. 5mm/year), one centimeter of deformation in the claybox is analogous to 140 to 280kya of geologic time (mean = 210kya). In a fast moving system (i.e. 45mm/year), one centimeter of deformation in the claybox is analogous to 15.5 to 31 kya of geologic time (mean = 23.35kya). The range in represented geologic time for one particular slip rate is due to the range of clay strength (1cm in claybox = 0.7-1.4km in crust). With this knowledge, we can better contextualize our results using crustal observations.

2.6.2.1 Walker Lane

We can apply observations from the claybox to the actively deforming Walker Lane in eastern California and western Nevada (Faulds et al., 2005). Offset Oligocene paleovalleys and decreasing dextral displacement northward indicate Walker Lane is propagating northwards into Nevada (Faulds et al., 2005). At the northern extent of Walker Lane, workers observe minor NW striking faults with minimal displacement within a diffuse zone of distributed shear and normal faulting at the most northern point.

Some of the small, dextral faults in the northern Walker Lane are abandoned (Faulds et al., 2005). The current state of the northern most Walker Lane could be classified as stage 3 of fault development as classified in the results of this paper. Deformation is still diffuse and with some faults, but no continuous fault surface exists at the current state. Based on the long term slip rate estimates along Walker Lane of 2-10mm/year, and observing stage 3 persists for about 2 cm of plate displacement (in experiments UPK, UEN and UEK), we can estimate stage 3 will persist in northern Walker Lane for about 200my to 1my. Dextral deformation is estimated to have begun about 3-9Ma, progressing northwards fairly slowly. It is unclear how long this northern extent of Walker Lane has been in stage 3, but we can perhaps expect a localized fault to organize from within this northern diffuse area of distributed shear.

We could estimate the strike-slip efficiency of the entire system to better understand the active initiation in the northern part of Walker Lane. The entire system is estimated to accommodate 15-20% of the plate boundary motion between the Pacific and North American plates (Faulds et al., 2006). The plate rate at this boundary is about 45 mm/year (Demets et al., 2010). As such, Walker Lane has about 6.8-9mm/year applied tectonic loading. Given the range of a 2-10 mm/year long term slip rate, strike-slip efficiency is difficult to determine because of the range in slip rate. As endmembers, the system could be as inefficient as 22%, or as efficient as 100%. Considering a slip rate of 10mm/year in a system that has a maximum of 9mm of applied loading per year would yield an implausible strike-slip efficiency of 110%. If the system is only 22% strike-slip efficient, we should expect the system to rapidly increase slip rate (maybe with the proposed 2-10mm/year range) and therefore increase in strike-slip efficiency in stage 2 of

fault initiation. The possibility of the Walker Lane system being 100% efficient is very low, considering the Walker Lane is a series of discontinuous, overlapping faults (i.e. stage 3). With these observations, the strike-slip efficiency of the entire Walker Lane is likely between 60-90% with much variation along the fault dependent on local fault roughness. Walker Lane could be in a stage of initiation where the entire fault system is efficient along its length, with local inefficiencies in the north where strain is still localizing to form a continuous, throughgoing fault. Over much more geologic time, the Walker Lane may become a localized plate boundary as a continuous fault surface develops.

2.6.2.2 Dead Sea Fault

Some previous work has suggested that a change in plate motion is required to partition strain with a completely strike-slip fault paired with an oblique-slip fault within a stepover along a strike-slip fault (i.e. Gomez et al., 2007). In this system, a restraining bend ($15^\circ \leq \theta \leq 20^\circ$) has a throughgoing fault accommodating strike-slip, and some splays accommodating oblique-slip. In this way, the system is considered completely strain partitioned, and is hypothesized to have been behaving in this way throughout the Cenozoic (Gomez et al., 2007). In order to have the currently strain partitioned system, Gomez et al. (2007) hypothesize that the Arabian plate must have changed direction. The Arabian plate is currently moving NNW-SSE, but if the plate motion was moving more N-S relative to the Sinai plate during the initiation of the restraining bend, more deformation would have been accommodated off the fault with significant components of distributed shear, block rotation and less uplift. The current tectonic setting accommodates convergence as uplift in the Lebanon Range, perhaps by increased

obliquity of plate motion relative to the active fault traces if the Arabian plate did change direction. The change in plate direction is based upon observed counterclockwise rotation in the Lebanon range (Gomez et al., 2007). Based on observations of the evolution modeled restraining bends by Hatem et al. (in prep) and on results presented in this study, we see the progression from distributed shear to strain localization to high strike-slip efficiency without changing the plate motion vector. Additionally, Titus et al., 2011 observe vertical axis rotation along the northern San Andreas in California (USA). They state the off-fault deformation exhibited as differential motion between blocks caused by vertical axis rotation is cause enough to initiate a persistent restraining bend (Titus et al., 2011). Observing strain partitioning between strike-slip and oblique-slip/off-fault deformation in a restraining bend is not reason enough to assume a change in plate direction.

2.7 Conclusions

Strike-slip faults become efficient as strain localizes onto echelon (Reidel) shears, which later grow, link and partially abandon to form a central fault. Strike-slip initiation is dependent on depth of basal shear zone, style of basal detachment and presence of a preexisting fault. Strike-slip systems with a pre-cut fault rapidly gain efficiency; uncut experiments accommodate more off-fault deformation for longer in the experiment. Modeled faults exceed 90% strike-slip accommodation, meaning the modeled faults have 10% or less off-fault deformation within the system by the end of the experiment. Strike-slip systems improve efficiency rapidly initially, and slowly maximize efficiency within the system from high to very high. We observe a three stage process of strike-slip fault

initiation, including 1) diffuse deformation, 2) strain localization onto echelon faults, and 3) interaction between echelon faults to overlap, link and partially abandon, to grow a continuous fault surface. After stage 3, a continuous fault accommodates strike-slip within the modeled system. Strike-slip efficiency increases as shear zone width decreases. Interacting, overlapping faults are roughest during stage 3 of fault initiation. Stepovers in the system concentrate areas of counterclockwise deformation in an otherwise dextral, clockwise system. Modeled faults help contextualize crustal examples of strike-slip faults in terms of current mechanical behavior, timing of initiation, and kinematic interpretations of field observations.

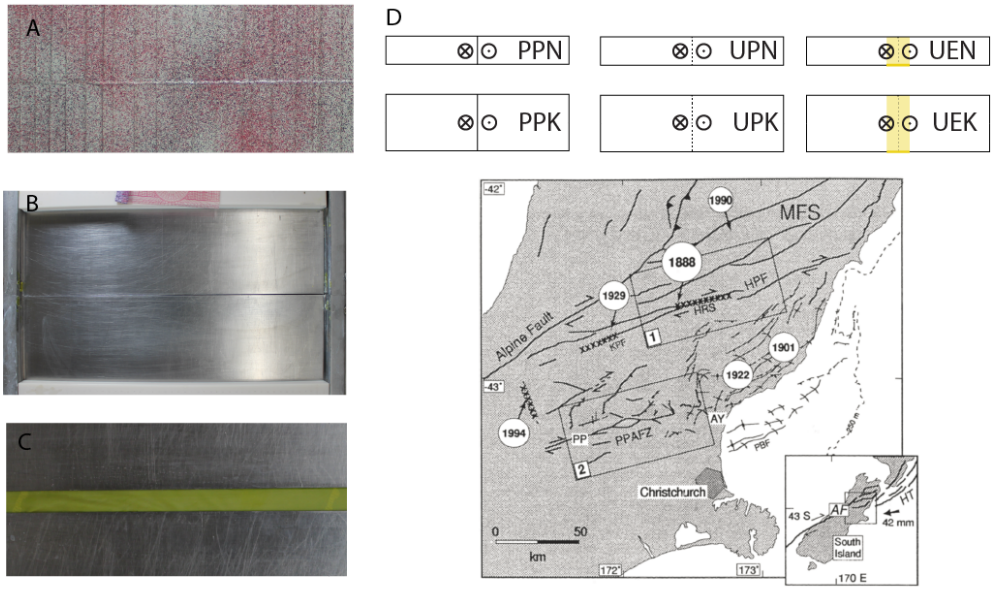

Figure 2.1 Experimental set-up and motivation

A) Pre-cut fault ready for displacement. Red and black sand helps to track pixels in PIV analysis. B) Basal plate set up for a localized basal shear experiment. Ruler = 15cm. C) Close up of basal plates set up for a distributed basal shear experiment. Width of yellow resistance band is 1.5 cm. D) Schematics showing each experiment with boundary conditions and three letter experiment name. Solid black line represents a pre-cut fault; dashed gray line represents an uncut fault. Yellow rectangles surrounding the gray dashed line show plates are set up as in figure C; no yellow rectangle indications the basal plates are set up as show in figure B. E) Figure 1 from Cowan et al., 1996 showing mature and immature fault systems in New Zealand. The Alpine fault in the north represents a more mature fault system compared to the younger Porter's Pass-to-Amberley Fault Zone (PPAFZ) in the south.

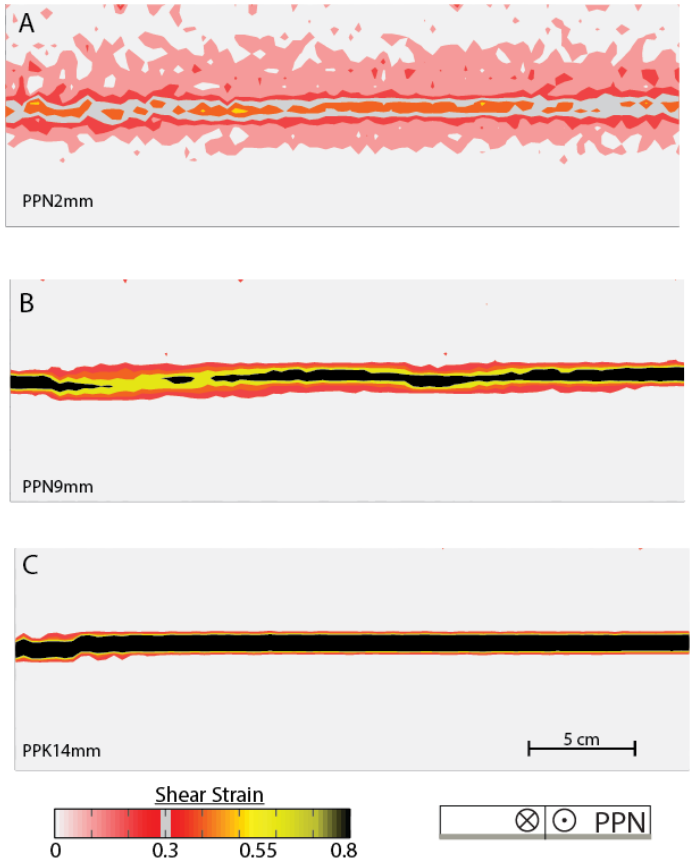

Figure 2.2 Shear strain maps of PPN

Shear strain localization in experiment PPN. Strain quickly localizes from a shear zone (A to B) onto a narrow fault trace (C).

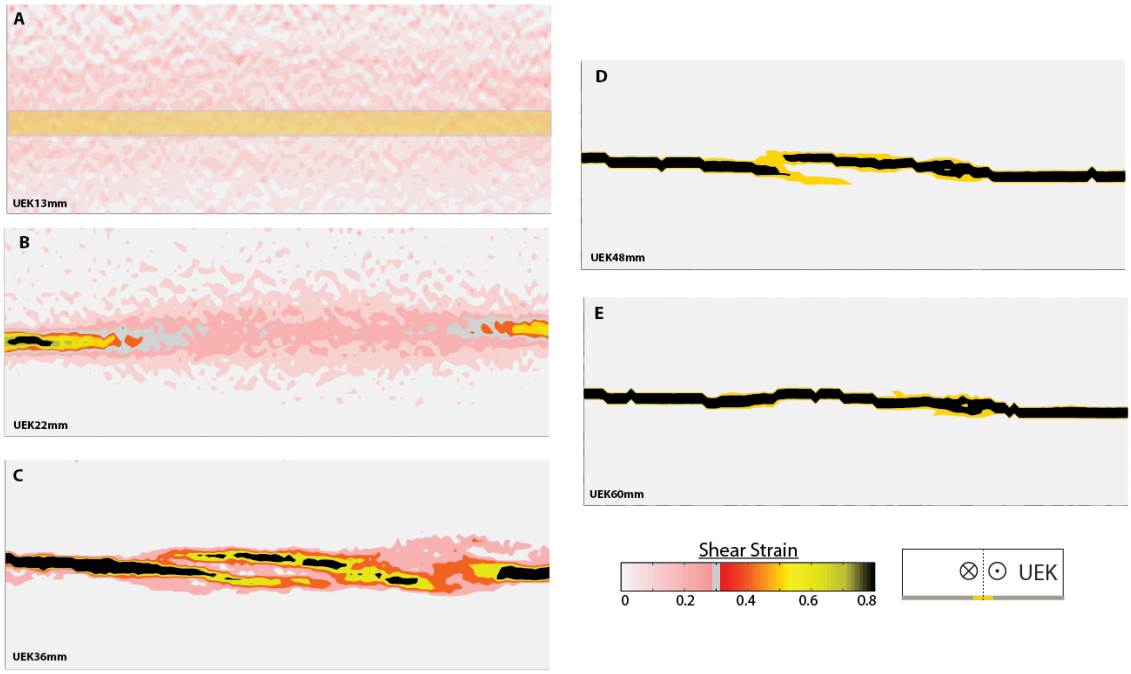

Figure 2.3 Shear strain maps of UEK

Shear strain localization in experiment UEK. Shear strain begins diffuse in a broad shear zone, decreasing in magnitude with distance away from the underlying elastic sheet. The elastic sheet is highlighted with a yellow rectangle in A. Strain localizes to a broad fault zone (B) containing echelon faults (C) that link (D) and form a localized, throughgoing fault (E).

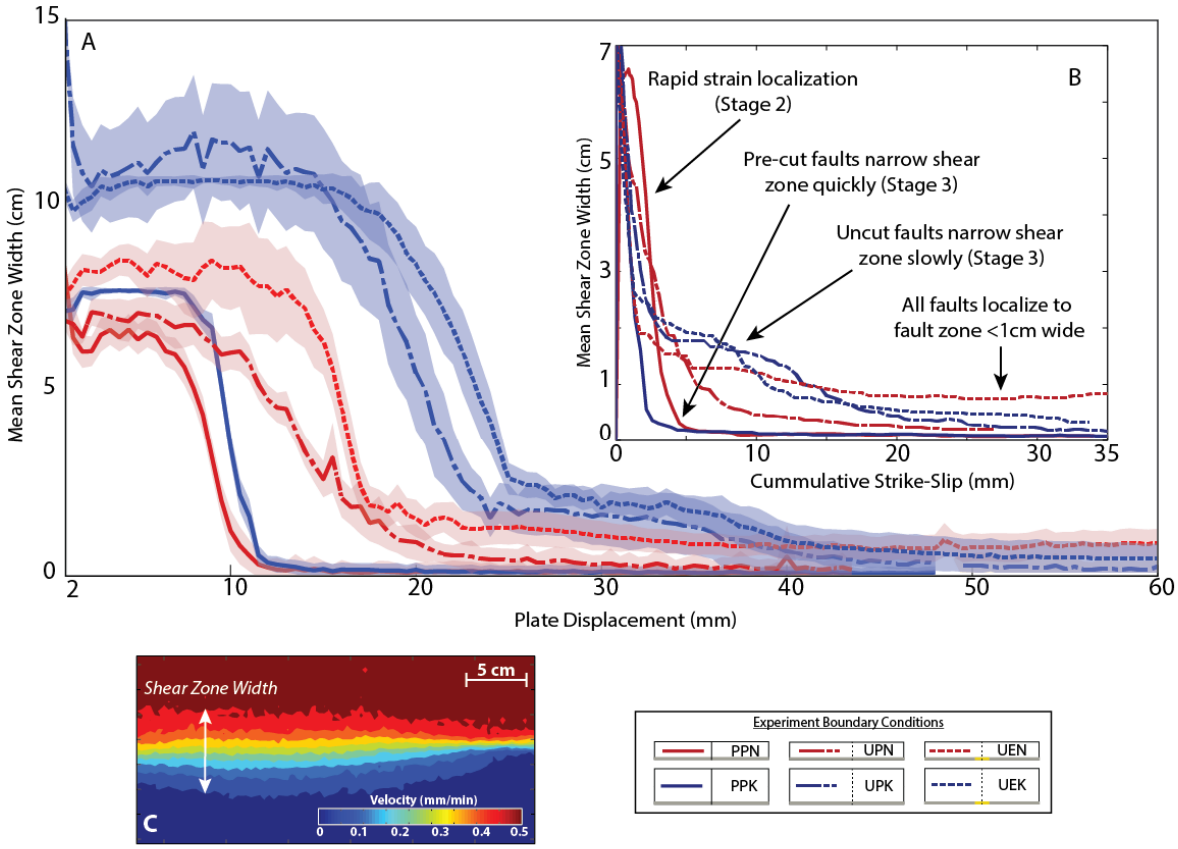

Figure 2.4 Shear zone width

Shear zone width of each experiment plotted against plate displacement, bounded by standard deviation (A). Shear zone width plotted against cumulative strike-slip within the experimental fault system is plotted in the inset. Shear zone width is defined in the map (C) as the changing width of the displacement zone (where displacement is nonzero and less than plate rate).

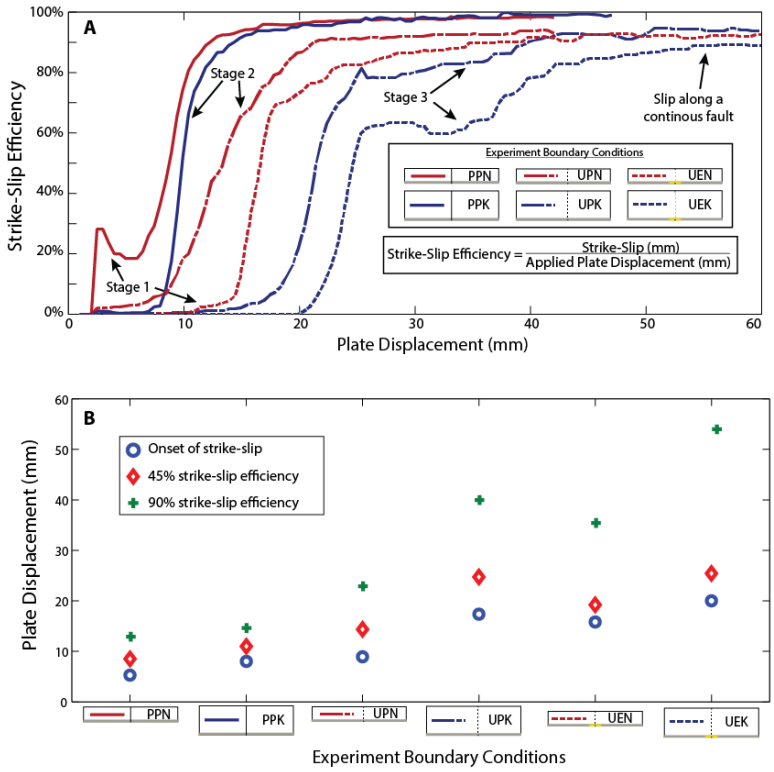

Figure 2.5 Strike-slip efficiency

A) Strike-slip efficiency versus plate displacement for various experiment boundary conditions. Both pre-cut and uncut experiments evolve to become at least 90% strike-slip efficient. Stages of shear zone development are denoted on strike-slip efficiency curves. B) Scatter plot of experiment boundary conditions versus the plate displacement at which each experiment achieves strike-slip efficiency milestones (nonzero, efficiency = 45%, efficiency = 90%). Faults become moderately efficient soon after the onset of slip, but require more applied plate displacement before becoming highly efficient. Faults with an elastic basal plate appear to propagate from within the claypack, and faults metal basal plates propagate upward from the basal plate; the onset of slip in UPK occurs at double the plate displacement of UPN, but not in UEK and UEN.

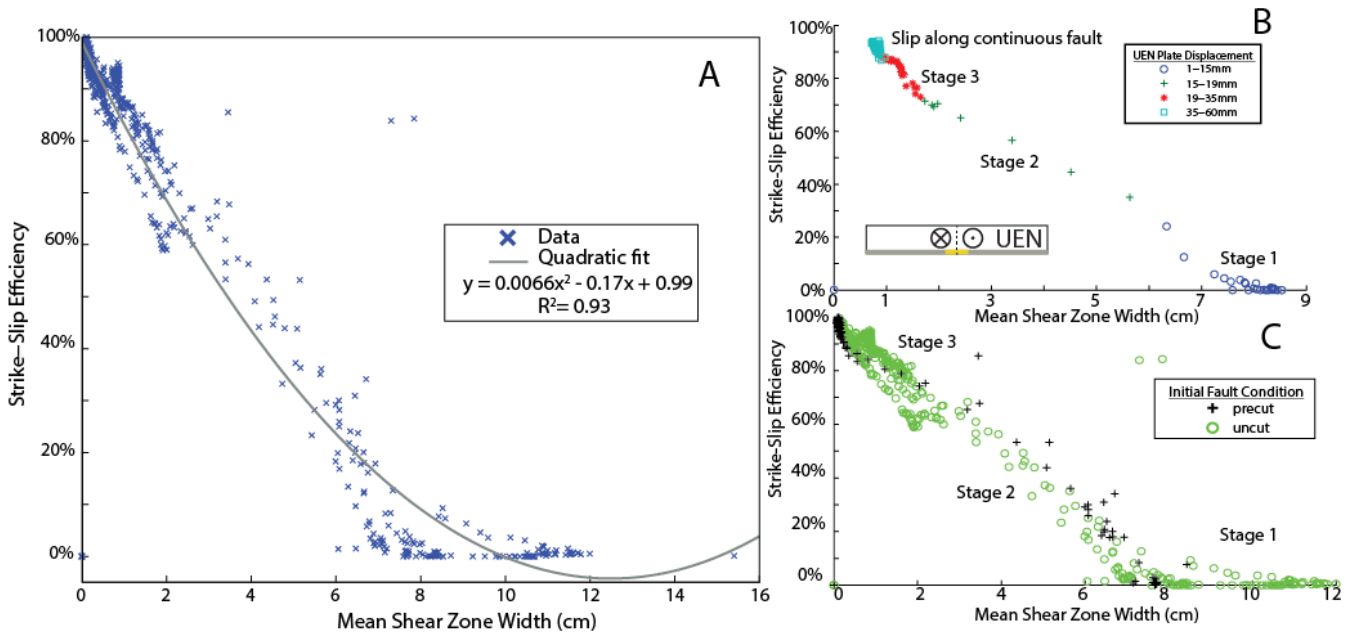

Figure 2.6 Strike-slip efficiency vs. shear zone width

A) Scatter plot of shear zone width versus strike-slip efficiency shows a strong anti-correlation between the two variables. Strike-slip efficiency increases as shear zone width decreases. R^2 of quadratic fit is 0.93. B) Delineating the stages of fault initiation for experiment UEN in the anti-correlation show how data are distributed throughout the fault system evolution. C) Pre-cut and uncut faults have slightly different distributions in stage 2 of fault initiation, showing the importance of preexisting structures on strain localization.

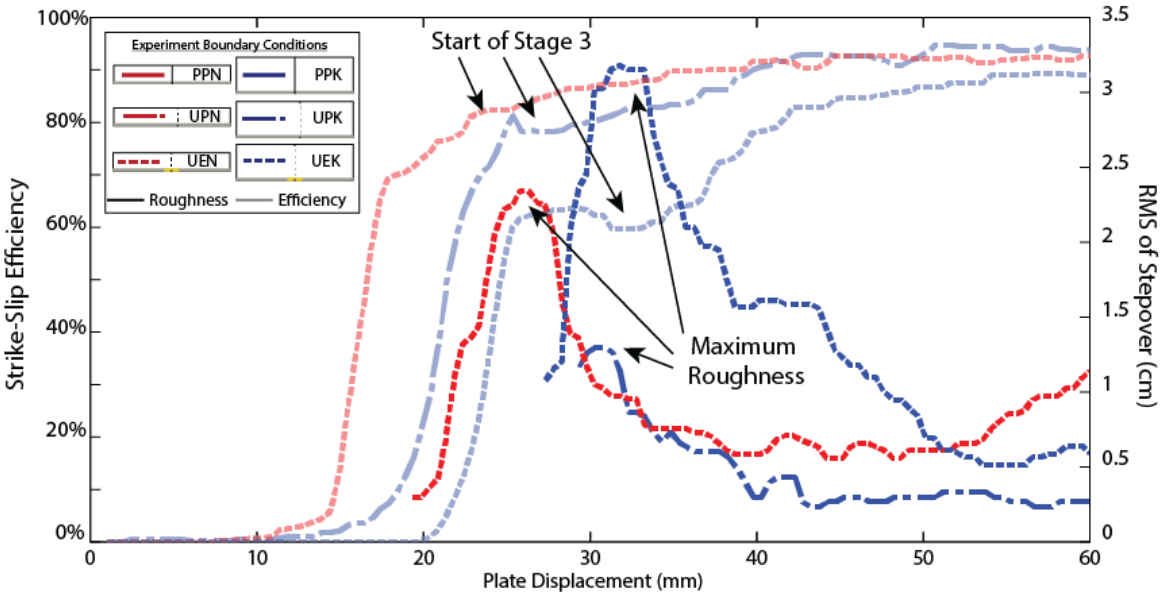

Figure 2.7 Fault roughness

Strike-slip efficiency and root mean square (RMS) of fault roughness (stepover amplitude) plotted throughout the experiments with observed stepovers. Stage 3 of strike-slip efficiency corresponds well to the roughest fault geometries observed in such models. RMS data is only plotted when faults are active (after onset of slip). Interacting faults reduce the rate at which faults become strike-slip efficient.

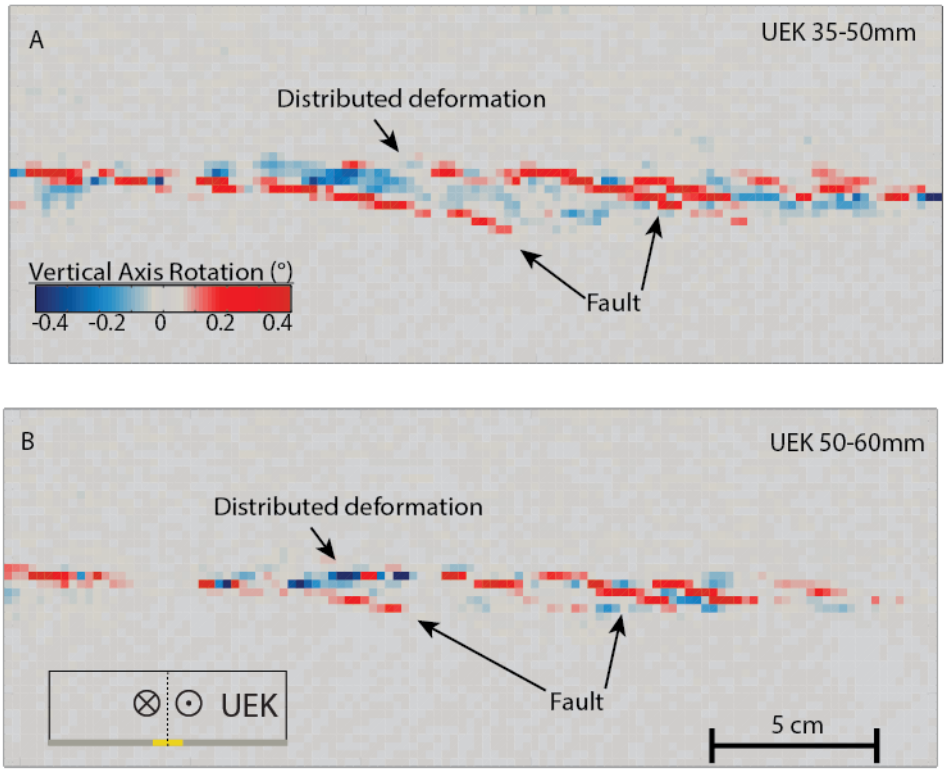

Figure 2.8 Vertical axis rotation of UEK

Spatial distribution of cumulative vertical axis rotation in experiment UEK. Faults are rotation clockwise (red), and distributed deformation rotates counterclockwise (blue). Counterclockwise rotation is more diffuse when the entire fault is rougher between the overlapping faults (A), and is more concentrated near the edges of the overlapping faults when the fault is relatively smooth (B).

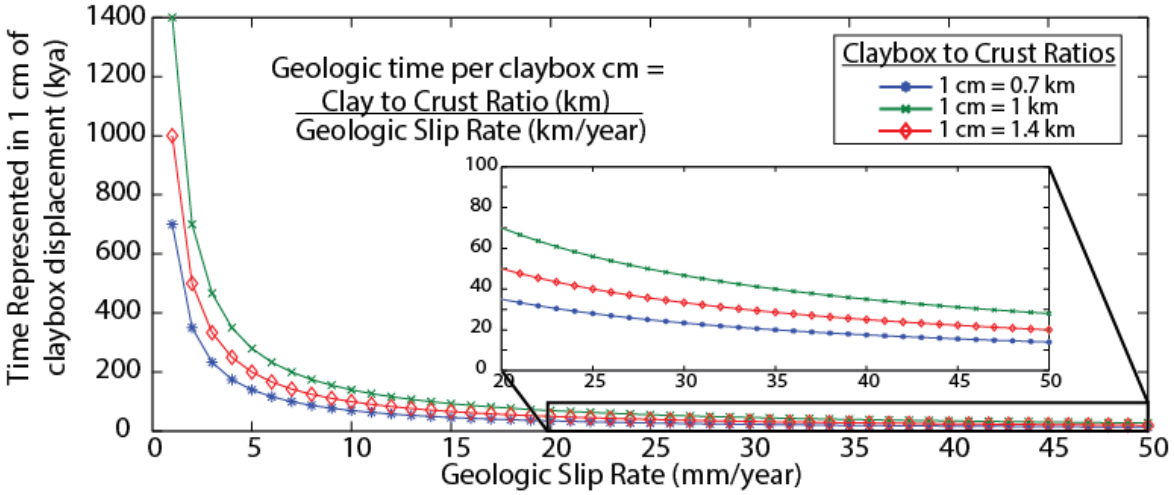

Figure 2.9 Temporal scaling relationships between clay and crust

Temporal scaling relationships between the claybox and the Earth's crust for a range of length scales. Crustal systems with slower geologic slip rates model the same amount of time with less applied plate displacement in the claybox compared to fast slipping systems.

2.8 References

Adam, J., J. L. Urai, B. Wieneke, K. Pfeiffer, N. Kukowski, J. Lohrmann, S. Hoth, W. Van Der Zee, and J. Schmatz. Shear Localisation and Strain Distribution during Tectonic Faulting—new Insights from Granular-flow Experiments and High-resolution Optical Image Correlation Techniques, *Journal of Structural Geology* 27.2 (2005): 283-301.

An, L-J and C.G. Sammis (1996), Development of strike-slip faults: shear experiments in granular materials and clay using a new technique, *Journal of Structural Geology*, 18, 1061-1077.

Caine, J.S, J.P Evans, and C.B Forster. "Fault zone architecture and permeability structure." Geology 24.11 (1996): 1025-1028.

Candela, T., F. Renard, M. Bouchon, A.Brouste, D. Marsan, J. Schmittbuhl, C. Voisin (2009), Characterization of fault roughness at various scales: Implications of three-dimensional high resolution topography measurements, *Pure and Applied Geophysics*, 166, 1817-1851.

Cochran, E.S., Y.G. Li, P.M. Shearer, S. Barbot, Y. Fialko, J.E. Vidale (2009), Seismic and geodetic evidence for extensive, long-lived fault damage zones, *Geology*, 37, 315-318.

Cooke, M. L., M.T. Schottenfeld, S.W. Buchanan (2013), Evolution of fault efficiency at restraining bends within wet kaolin analog experiments, *Journal of Structural Geology*, 51, 180-192.

Cooke, M. L., and N. J. van der Elst (2012), Rheologic testing of wet kaolin reveals frictional and bi-viscous behavior typical of crustal materials, Geophys. Res. Lett., 39.

Cowan, H., A. Nicol, P. Tonkin (1996), A comparison of historical and paleoseismicity in a newly formed fault zone and a mature fault zone, North Canterbury, New Zealand, *Journal of Geophysical Research*, 101, 6021-6036.

Demets, C., R.G. Gordon, D.F. Argus (2010), Geologically current plate motions, *Geophs. J. Int.*, 181, 1-80.

Dawson, T.E., S.F. McGill, T.K. Rockwell (2003), Irregular recurrence of paleoearthquakes along the central Garlock fault near El Paso Peaks, California, *Journal of Geophysical Research*, 108,

Dolan, J.F., D.D. Bowman, C.G. Sammis (2007), Long-range and long-term fault interactions in Southern California, *Geology*, 35, 855-858.

Eisenstadt, G., and D. Sims. "Evaluating Sand and Clay Models: Do Rheological Differences Matter?" *Journal of Structural Geology* (2005): 1399-412.

Faulds, J.E., C.D. Henry, N.H. Hinz (2005), Kinematics of the northern Walker lane: An incipient transform fault along the Pacific-North American plate boundary, *Geology*, 33, 505-508.

Gomez, F.,T. Nemer, C. Tabel, M Khawlie, M. Meghroui, M. Barazangi (2007), Strain Partitioning of Active Transpression Within the Lebanese Restraining Bend of the Dead Sea Fault (Lebanon and SW Syria), from Tectonics of Strike-Slip Restraining and Releasing Bends, Cunningham, W.D. and P. Mann (eds), Geol. Soc. Of London, 290, 285-303.

Henza, A., M. O. Withjack, and R. W. Schlische (2010), Normal-fault developmsent during two phases of non-coaxial extension: An experimental study, J. Struct. Geol., 32, 1656–1667.

Herbert, J.W., M.L. Cooke, M. Oskin, O.Difo (2014), How much can off-fault deformation contribute to the slip rate discrepancy within the eastern California shear zone?, Geology, 42, 71-75.

Herbert, J.W. and M.L. Cooke (2012), Sensitivity of the southern San Andreas fault system to tectonic boundary conditions and fault conditions, *Bulletin of Seismological Society of America*, 102, 2046-2062.

Mann, P. (2007) Global catalogue, classification and tectonic origins of restraining and releasing bends on active and ancient strike-slip fault systems, , from *Tectonics of Strike-Slip Restraining and Releasing Bends,* Cunningham, W.D. and P. Mann (eds), Geol. Soc. Of London, 290, 13-142.

Schlische, Roy W., Martha O. Withjack, and Gloria Eisenstadt. "An Experimental Study of the Secondary Deformation Produced by Oblique-slip Normal Faulting." *American Association of Petroleum Geologists Bulletin* 86.5 (2002): 885-906.

Schmittbuhl, J., S. Gentier, S. Roux (1993), Field Measurements of the roughness of fault surfaces, *Geophysical Research Letters,* 20, 639-641.

Segall, P. and D.D. Pollard (1983), Nucleation and growth of strike-slip faults in granite, *Journal of Geophysical Research*, 88, 555-568.

Sharp, R.V. (1981), Variable rates of late Quaternary strike slip on the San Jacinto fault zone, southern California, *Journal of Geophysical Research*, 86, 1754-1762.

Shelef, E. and M. Oskin (2010) Deformation processes adjacent to active faults: Examples from eastern California, *Journal of Geophysical Research*, 115.

Titus, S.J., S. Crump, Z. McGuire, E. Horsman, B. Housen (2011), Using vertical axis rotations to characterize off- fault deformation across the San Andreas fault system, central California, *Geology*, 39, 711-714.

Titus, S.J., B. Housen, B. Tikoff (2007), A kinematic model for the Rinconada fault system in central California based on structural analysis of *en echelon* folds and paleomagnetism, *Journal of Structural Geology*, 29, 961-982.

Wakabayashi, J. (2007), Stepovers that migrate with respect to affected deposits: field characteristics and speculation on some details of their evolution, from *Tectonics of Strike-Slip Restraining and Releasing Bends,* Cunningham, W.D. and P. Mann (eds), Geol. Soc. Of London, 290, 169-188.

Wilcox, R.E., T.P. Harding, D.R. Seely (1973), Basic Wrench Tectonics, *AAPG Bulletin*, 57, 74-96.

REFERENCES

Ackerman, R.V., R.W. Schlische, and M. O. Withjack. "The Geometric and Statistical Evolution of Normal Fault Systems: An Experimental Study of the Effects of Mechanical Layer Thickness on Scaling Laws." *Journal of Structural Geology*, 23 (2001): 1803-819.

Adam, J., J. L. Urai, B. Wieneke, K. Pfeiffer, N. Kukowski, J. Lohrmann, S. Hoth, W. Van Der Zee, and J. Schmatz. Shear Localisation and Strain Distribution during Tectonic Faulting—new Insights from Granular-flow Experiments and High-resolution Optical Image Correlation Techniques, *Journal of Structural Geology* 27.2 (2005): 283-301.

Adrian, R. J., and J.Westerweel. *Particle Image Velocimetry*. New York: Cambridge UP, 2011.

An, L-J and C.G. Sammis (1996), Development of strike-slip faults: shear experiments in granular materials and clay using a new technique, *Journal of Structural Geology*, 18, 1061-1077.

Cadell, H.M. 1889. Experiment researches in mountain building. *Transactions of the Royal Society of Edinburg*, 1, 339-343.

Caine, J.S, J.P Evans, and C.B Forster. "Fault zone architecture and permeability structure." Geology 24.11 (1996): 1025-1028.

Candela, T., F. Renard, M. Bouchon, A.Brouste, D. Marsan, J. Schmittbuhl, C. Voisin (2009), Characterization of fault roughness at various scales: Implications of three-dimensional high resolution topography measurements, *Pure and Applied Geophysics*, 166, 1817-1851.

Cloos, H. (1928), Experimente zur inneren Tektonik, Zen. Min., Geol. Pal., 1928B, 609–621.

Cochran, E.S., Y.G. Li, P.M. Shearer, S. Barbot, Y. Fialko, J.E. Vidale (2009), Seismic and geodetic evidence for extensive, long-lived fault damage zones, *Geology*, 37, 315-318.

Cooke, M.K. and L.C. Dair (2011), Simulating the recent evolution of the southern big bend of the San Andreas fault, Southern California, *Journal of Geophysical Research*, 116.

Cooke, M. L., M.T. Schottenfeld, S.W. Buchanan (2013), Evolution of fault efficiency at restraining bends within wet kaolin analog experiments, *Journal of Structural Geology*, 51, 180-192.

Cooke, M. L., and N. J. van der Elst (2012), Rheologic testing of wet kaolin reveals frictional and bi-viscous behavior typical of crustal materials, Geophys. Res. Lett., 39.

Cooke, M.L. and S. Murphy (2004), Assessing the work budge and efficiency of fault systems using mechanical models, J. Geophys. Res., 109.

Cowan, H., A. Nicol, P. Tonkin (1996), A comparison of historical and paleoseismicity in a newly formed fault zone and a mature fault zone, North Canterbury, New Zealand, *Journal of Geophysical Research,* 101, 6021-6036.

Cunningham, W.D., and P. Mann (2007), (eds) Tectonics of Strike-Slip Restraining and Releasing Bends, Geol. Soc. Of London, Special Publications, 290, 1-12.

Cunningham, W.D., Structural and topographic characteristics of restraining bend mountain ranges of the Altai, Gobi Altai and easternmost Tien Shan, from Tectonics of Strike-Slip Restraining and Releasing Bends, Cunningham, W.D. and P. Mann (eds), Geol. Soc. of London, 290, 219-238.

Curren, I.S. and P. Bird (2014), Formation and suppression of strike-slip fault systems, *Pure and Applied Geophysics*, 1-20.

DeGroot, D.J., Lunne, T., 2007. Measurement of Remoulded Shear Strength. Norwegian Geotechnical Institute. Report 20061023-1.

Del Castello, M., G.A. Pini, K.R. McClay (2004), Effect of unbalanced topography and overloading on Coulomb wedge kinematics: Insights from sandbox modeling, *Journal of Geophysical Research*, 109.

Demets, C., R.G. Gordon, D.F. Argus (2010), Geologically current plate motions, *Geophs. J. Int.*, 181, 1-80.

Dawson, T.E., S.F. McGill, T.K. Rockwell (2003), Irregular recurrence of paleoearthquakes along the central Garlock fault near El Paso Peaks, California, *Journal of Geophysical Research*, 108,

Dolan, J.F., D.D. Bowman, C.G. Sammis (2007), Long-range and long-term fault interactions in Southern California, *Geology*, 35, 855-858.

Eisenstadt, G., and D. Sims. "Evaluating Sand and Clay Models: Do Rheological Differences Matter?" *Journal of Structural Geology* (2005): 1399-412.

Faulds, J.E., C.D. Henry, N.H. Hinz (2005), Kinematics of the northern Walker lane: An incipient transform fault along the Pacific-North American plate boundary, *Geology*, 33, 505-508.

Fialko, Y., L. Rivera, H. Kanamori (2005), Estimate of differential stress in the upper crust from variations in topography and strike along the San Andreas fault, *Geophys. J. Int*, 160, 527-532.

Gomez, F.,T. Nemer, C. Tabel, M Khawlie, M. Meghroui, M. Barazangi (2007), Strain Partitioning of Active Transpression Within the Lebanese Restraining Bend of the Dead Sea Fault (Lebanon and SW Syria), from Tectonics of Strike-Slip Restraining and Releasing Bends, Cunningham, W.D. and P. Mann (eds), Geol. Soc. Of London, 290, 285-303.

Haeussler, P.J. (2008), An overview of the neotectonics of interior Alaska: Far-field deformation from the Yakutat Microplate Collision, *Active Tectonics an seismic potential of Alaska*, AGU Monograph Series 109, 83-108.

Henza, A., M. O. Withjack, and R. W. Schlische (2010), Normal-fault developmsent during two phases of non-coaxial extension: An experimental study, J. Struct. Geol., 32, 1656–1667.

Herbert, J.W., M.L. Cooke, M. Oskin, O.Difo (2014), How much can off-fault deformation contribute to the slip rate discrepancy within the eastern California shear zone?, Geology, 42, 71-75.

Herbert, J.W. and M.L. Cooke (2012), Sensitivity of the southern San Andreas fault system to tectonic boundary conditions and fault conditions, *Bulletin of Seismological Society of America*, 102, 2046-2062.

Mann, P. (2007) Global catalogue, classification and tectonic origins of restraining and releasing bends on active and ancient strike-slip fault systems, , from *Tectonics of Strike-Slip Restraining and Releasing Bends,* Cunningham, W.D. and P. Mann (eds), Geol. Soc. Of London, 290, 13-142.

Malavielle, J. (2010), Impact of erosion, sedimentation, and structural heritage on the structure and kinematics of orogenic wedges: Analog models and case studies, *GSA Today*, 20, 4-10.

Matti, J. C., and D. M. Morton (1993), Paleogeographic evolution of the San Andreas fault in Southern California: A reconstruction based on a new cross-fault correlation, Mem. Geol. Soc. Am., 178, 107– 159.

Matti, J. C., D. M. Morton, and B. F. Cox (1992), The San Andreas fault system in the vicinity of the central Transverse Ranges province, Southern California, U.S. Geol. Surv. Open File Rep., 92–0354.

McClay, K., and M. Bonora (2001), Analog models of restraining stepovers in strike-slip fault systems, *AAPG Bulletin*, 85 (2), 233-260.

McGill, S.D., L.A. Owen, R.J. Weldon II, K.J. Kendrick (2013), Latest Pleistocene and Holocene slip rate for the San Bernardino strand of the San Andreas fault, Plunge Creek, Southern California: Implications for strain partitioning within the southern San Andreas fault system for the last ~35 k.y., GSA Bulletin, 125 (1), 48-72.

Mitra, S. and D. Paul (2011), Structural geometry and evolution of releasing and restraining bends: Insights from laser-scanned experimental models, AAPG Bulletin, 95 (7), 1147-1180.

Oertel, G. (1965), The mechanism of faulting in clay experiments, Tectonophysics, 2, 343-393.

Paul, D., and S. Mitra (2013), Experimental models of transfer zones in rift systems, *AAPG Bulletin*, 97, 759-780.

Reilinger, R., et al. (2006), GPS constraints on continental deformation in the Africa-Arabia-Eurasia continental collision zone and implications for the dynamics of plate interactions, J. Geophys. Res., 111,

Schlische, Roy W., Martha O. Withjack, and Gloria Eisenstadt. "An Experimental Study of the Secondary Deformation Produced by Oblique-slip Normal Faulting." *American Association of Petroleum Geologists Bulletin* 86.5 (2002): 885-906.

Schmittbuhl, J., S. Gentier, S. Roux (1993), Field Measurements of the roughness of fault surfaces, *Geophysical Research Letters,* 20, 639-641.

Segall, P. and D.D. Pollard (1983), Nucleation and growth of strike-slip faults in granite, *Journal of Geophysical Research*, 88, 555-568.

Sharp, R.V. (1981), Variable rates of late Quaternary strike slip on the San Jacinto fault zone, southern California, *Journal of Geophysical Research*, 86, 1754-1762.

Shelef, E. and M. Oskin (2010) Deformation processes adjacent to active faults: Examples from eastern California, *Journal of Geophysical Research*, 115.

Scholz, C. H. (2002). *The mechanics of earthquakes and faulting*. Cambridge University Press.

Slominski, C., Niedostatkiewicz, M., & Tejchman, J. (2007). Application of particle image Velocimetry (PIV) for deformation measurement during granular silo flow. *Powder Technology*, *173*(1), 1-18.

Swanson, M.T. (2005), Geometry and kinematics of adhesive wear in brittle strike-slip fault zones, *Journal of Structural Geology*, 27, 871-887.

Titus, S.J., S. Crump, Z. McGuire, E. Horsman, B. Housen (2011), Using vertical axis rotations to characterize off- fault deformation across the San Andreas fault system, central California, *Geology*, 39, 711-714.

Titus, S.J., B. Housen, B. Tikoff (2007), A kinematic model for the Rinconada fault system in central California based on structural analysis of *en echelon* folds and paleomagnetism, *Journal of Structural Geology*, 29, 961-982.

Wakabayashi, J., J.V. Hengesh, T.L. Sawyer (2004), Four-dimensional transform fault processes: progressive evolution of step overs and bends, Tectonophysics, 392, 279-301.

Wakabayashi, J. (2007), Stepovers that migrate with respect to affected deposits: field characteristics and speculation on some details of their evolution, from *Tectonics of Strike-Slip Restraining and Releasing Bends,* Cunningham, W.D. and P. Mann (eds), Geol. Soc. Of London, 290, 169-188.

Withjack, M.O., Q.T. Islam, and P.R. La Pointe. "Normal Faults and Their Hanging-Wall Deformation: An Experiment Study." *American Association of Petroleum Geologists Bulletin* 79.1 (1995): 1-18.

Wilcox, R.E., T.P. Harding, D.R. Seely (1973), Basic Wrench Tectonics, *AAPG Bulletin*, 57, 74-96.

Yule, D. and K. Sieh (2003), Complexities of the San Andreas near San Gorgonio Pass: Implications for large earthquakes, Journal *of Geophysical Research*, 108.

Veenstra, E., D.H. Christensen, G.A. Abers, A. Ferris (2006), Crustal thickness variation in south-central Alaska, *Geology*, 34, 781-784.